The asymmetric eddy-background flow interaction in the North Pacific storm track

Article

Accepted Version

Quarterly Journal of the Royal Meteorological Society
A journal of the atmospheric sciences and physical oceanography
RMetS

The asymmetric eddy-background flow interaction in the North Pacific storm track

Journal:	*QJRMS*
Manuscript ID	QJ-18-0042.R2
Wiley - Manuscript type:	Research Article
Date Submitted by the Author:	n/a
Complete List of Authors:	Zhao, Yuan-Bing; Nanjing University of Information Science and Technology, Liang, X. San; Nanjing University of Information Science and Technology Guan, Zhaoyong; Nanjing University of Information Science and Technology Hodges, Kevin; The University of Reading, Dept. of Meterology
Keywords:	eddy-mean flow interaction, extra-tropical cyclone, feature tracking, multiscale energetics, canonical energy transfer
Country Keywords:	China

The asymmetric eddy-background flow interaction in the North Pacific storm track

Yuan-Bing Zhao[1], X. San Liang[12*], Zhaoyong Guan[1], and Kevin I. Hodges[3]

[1] School of Atmospheric Sciences, Nanjing University of Information Science and Technology, Nanjing, Jiangsu, 210044, China

[2] School of Marine Sciences, Nanjing University of Information Science and Technology, Nanjing, Jiangsu, 210044, China

[3] Department of Meteorology, National Centre for Earth Observation, University of Reading, Reading, UK

Correspondence

X. San Liang, Nanjing Center for Ocean-Atmosphere Dynamical Studies, Nanjing, Jiangsu, 210044, China.

E-mail: x.san.liang@gmail.com

Running head

Asymmetric eddy-mean flow interaction

Abstract

Using a recently developed methodology, namely, the multiscale window transform (MWT), and the MWT-based theory of canonical transfer and localized multiscale energetics analysis, we investigate in an eddy-following way the nonlinear eddy-background flow interaction in the North Pacific storm track, based on the ERA40 reanalysis data from ECWMF. It is found that more than 50% of the storms occur on the northern flank of the jet stream, about 40% are around the jet center, and very few (less than 5%) happen on the southern flank. For storms near or to the north of the jet center, their interaction with the background flow is asymmetric in latitude. In higher latitudes, strong downscale canonical available potential energy transfer happens, especially in the middle troposphere, which reduces the background baroclinicity and decelerates the jet; in lower latitudes, upscale canonical kinetic energy transfer intensifies at the jet center, accelerating the jet and enhancing the middle-level baroclinicity. The resultant effect is that the jet strengthens but narrows, leading to an anomalous dipolar pattern in the fields of background wind and baroclinicity. For the storms on the southern side of the jet, the baroclinic canonical transfer is rather weak. On average, the local interaction begins from about 3 days before a storm arrives at the site of observation, achieves its maximum as the storm arrives, and then weakens.

KEYWORDS

Eddy-mean flow interaction, extra-tropical cyclone, feature tracking, multiscale energetics, canonical energy transfer

1. Introduction

Eddy-mean flow interaction is one of the central issues in dynamical meteorology. In the atmosphere, a typical site of eddy-mean flow interaction is the midlatitude storm track (Blackmon, 1976; Chang and Orlanski, 1993; Hoskins and Valdes, 1990). It has been shown that the atmospheric storm track generally coincides with the tropospheric jet, where the baroclinicity is the strongest (e.g., Chang et al., 2002; Lee and Kim, 2003). Within the storm track, synoptic eddies are often generated in the jet and then interact with it.

There is a long history of studies on the interaction between midlatitude synoptic eddies and the jet stream. In most early studies, the focus was on the theoretical aspects based on idealized models, e.g., those with small-amplitude perturbations in the form of sinusoidal waves and a zonally homogeneous, stationary background flow (in many cases also meridionally independent) (Andrews and McIntyre, 1978; Charney and Drazin, 1961; Dickinson, 1969; Eliassen and Palm, 1961; Lindzen and Holton, 1968; Plumb, 1985). However, in the real atmosphere the background flow is by nature temporally varying and zonally asymmetric; especially in midlatitudes, due to the large scale topography and land-sea contrasts (e.g., Lee and Kim, 2003; Li and Wettstein, 2011), whilst the eddies are rather localized in space and time with finite amplitudes (Blackmon

et al., 1984; Catto et al., 2010; Chang, 1993; Lim and Wallace, 1991; Simmons and Hoskins, 1978). In more recent studies, with the advent of observational and reanalysis data, discrepancies have been found between the previously proposed theories and the observations. For example, based on the previous theories it is supposed that baroclinic energy transfer associated with baroclinic instability is bottom-trapped (Edmon et al., 1980; Green, 1960; Hoskins et al., 1985; Lindzen and Farrell, 1980; Pierrehumbert and Swanson, 1995), whereas observational energetics diagnostics have implied that midlatitude synoptic systems have their maximum baroclinic energy transfer in middle levels (e.g., Chang et al., 2002). The spatial structure of the interaction is still a problem yet to be explored.

During the past two decades, eddy-mean flow interaction has been extensively discussed, especially in studies of annular modes (Barnes and Hartmann, 2011; Burrows et al., 2017; Chen and Plumb, 2009; Gerber and Vallis, 2007; Kidston et al., 2010; Kidston and Vallis, 2012; Lorenz, 2014; Lorenz and Hartmann, 2001; Robinson, 2000; Zhang et al., 2012, to name but a few). But, most of these studies have focused on the zonal-mean and climatologically statistical aspects. Rarely considered is the interaction between a typical individual eddy and the mean flow, except for a few studies such as Gerber and Vallis (2007), who argued that if the eddy is generated in the jet, the vertical wind shear is first reduced by the heat flux in the baroclinic development stage, and then in the decaying stage the jet is strengthened by upgradient momentum transfer through the wave meridional propagation (the net propagation of baroclinic wave activity away

from the jet gives momentum fluxes into the jet). On the whole, the jet structure is maintained in the presence of surface friction. Alternatively, if the eddy is growing on the shoulders of the jet, the baroclinic development stage is similar to that of the eddy growing in the jet. However, the meridional wave propagation is then limited aloft, and, as a result, the shear is reduced locally rather than over the entire baroclinic zone. Similar studies are also reported in Zhang et al. (2012) based on an idealized β-plane quasi-geostrophic model. As remarked by Vallis and Gerber (2008), the applicability of these results to the real atmosphere still needs verification.

We remark that, earlier on, a classical way to look at the eddy-mean flow interaction is with the "barotropic generation rate (Mak and Cai 1989; Cai and Mak 1990; Rivière et al. 2003) and "barocilinc generation rate" (Cai and Mak 1990; Rivière et al. 2004). The merit of this method is that if the eddy structure, the deformation of the jet, and the positional relationship between the eddy and the jet are known, then the energy exchange between the jet and the eddy can be easily determined (especially with the barotropic generation rate). But here this method is difficult to be applied, as it is derived in the quasi-geostrophic (QG) framework with the small amplitude assumption; besides, it does not tell how eddies would modify the mean flow.

In this study we apply a newly developed methodology, which is capable of handling these nonlinear problems in a generic sense, to diagnose the two-way interactions between individual midlatitude synoptic eddies and the background flow in an eddy-following way, in the hope of unraveling what is really happening locally in the

North Pacific storm track. The methodology includes a functional analysis apparatus, namely, the Multiscale Window Transform (MWT, Liang and Anderson 2007), and the MWT-based localized multiscale energy and vorticity analysis (MS-EVA, Liang 2016).

The rest of this paper is organized as follows. Section 2 describes the data used in this study. In section 3, we briefly introduce the MWT, MS-EVA, and the Lagrangian tracking and compositing method, and in section 4, we set up the MS-EVA application with the data. In the following sections (5, 6, 7, and 8), the composite reconstructed fields and a detailed eddy-mean flow interaction analysis are presented. The study is summarized in section 9.

2. Data

We use for our study the 40-year European Centre for Medium-Range Weather Forecasts (ECWMF) ReAnalysis (ERA40) dataset (Uppala et al., 2005), which is constrained by observations using a three-dimensional variational (3D-Var) data assimilation system. It has been used because of its length (45 years), spatial resolution (approximately $1.1° \times 1.1°$ in the tropics (T159), 35 vertical levels below 100 hPa), and temporal resolution (6 h). More information can be found at http://apps.ecmwf.int/datasets/data/era40-daily/levtype=pl/. Here we need the velocity components (u, v, and ω), geopotential (ϕ), and temperature (T) for the whole period from September 1957 to July 2002.

3. Methodology

3.1 Localized multiscale energetics analysis

The major research methodology for this study is the multiscale window transform (MWT) by Liang and Anderson (2007), and the MWT-based theory of canonical transfer (Liang 2016) and localized multiscale energy and vorticity analysis (MS-EVA) by Liang and Robinson (2005), which has been applied successfully in many atmosphere-ocean problems (e.g., Ma and Liang, 2017; Xu and Liang 2017). This section is just a short introduction of the concepts; more details are furnished in Appendix A. For a recently updated comprehensive introduction, refer to Liang (2016).

The MWT is a functional analysis tool that helps decompose a function space into a direct sum of several mutually orthogonal subspaces, each with an exclusive range of time scales, while preserving its local properties. Such a subspace is termed a *scale window* or simply a *window*. One may have as many windows as needed. In this study, we mainly use two, namely, a low-frequency basic-flow window (or background flow window) and a synoptic-scale window (or transient window); we will also use a three-window decomposition for testing purpose. For easy reference, they are denoted and will be referred to as windows $\varpi = 0, 1, \ldots$ Given a time series $T(t)$ with N steps, application of MWT yields two types of quantities: one is the MWT transform coefficients, $\hat{T}_n^{\sim\varpi}$ $(n = 1, 2, \cdots, N,$ corresponding to the time location in t), another the multiscale window reconstruction (MWR), $T^{\sim\varpi}(t)$. $T^{\sim\varpi}(t)$ is just like the

low/high-pass filtered quantity. For example, in the two-window decomposition in this study, the series $T(t)$ is decomposed into $T = T^{\sim 0}(t) + T^{\sim 1}(t)$, where $T^{\sim 0}$ stands for the background field, and $T^{\sim 1}$ the transient (or synoptic) eddy field. MWT and MWR form a transform-reconstruction pair, but they are distinctly different concepts, with the former defined in phase space while the latter in physical space (here *t*), just like the Fourier transform and inverse Fourier transform. The MWR of *T(t)* on the synoptic-scale window, for example, corresponds to a high-pass filtered signal. The lack of transform coefficient $\hat{T}_n^{\sim \varpi}$ in traditional filters makes it impossible to represent multiscale energy[1]. The common practice that simply takes multiscale energy as the square of filtered variables is a conceptual mistake which, unfortunately, has frequently appeared in the literature. But here with $\hat{T}_n^{\sim \varpi}$ it has been established that multiscale energy can be precisely represented as the product of the MWT coefficients (up to some constant multiplier). For example, the transient eddy energy extracted from *T(t)* is simply $\left(\hat{T}_n^{\sim 1}\right)^2$ multiplied by some constant.

With MWT, the available potential energy (APE) and kinetic energy (KE) densities on window ϖ at time location *n*, written as A_n^{ϖ} and K_n^{ϖ}, can be obtained, and their evolution equations derived by applying MWT to the primitive governing equations. Details are referred to Appendix A; the following is a symbolic representation (location *n* in the subscript omitted henceforth for simplicity):

[1] Note one cannot write it in terms of the filtered quantities such as $[T^{\sim 1}(\mathrm{t})]^2$, as multiscale energy is a concept in phase space. (Think about that in a Fourier spectrum.) Refer to Appendix A for more explanation.

$$\frac{\partial A^{\varpi}}{\partial t} + \nabla \cdot \mathbf{Q}_A^{\varpi} = \Gamma_A^{\varpi} - b^{\varpi} + \mathrm{S}_A^{\varpi} + \mathrm{F}_A^{\varpi} \quad (1)$$

$$\frac{\partial K^{\varpi}}{\partial t} + \nabla \cdot \mathbf{Q}_K^{\varpi} = \Gamma_K^{\varpi} - \nabla \cdot \mathbf{Q}_P^{\varpi} + b^{\varpi} + \mathrm{F}_K^{\varpi} \quad (2)$$

where $\varpi = 0$ and 1 stand for the two scale windows in this study, i.e., the basic flow window and the eddy window. The $\mathbf{Q}$'s with subscripts A, K, and P are, respectively, fluxes of APE, KE, and pressure, the Γ terms are the transfer of energy (APE or KE) to the designated scale window ϖ from other windows, b is buoyancy conversion, and F denotes the contribution from dissipation/diffusion. Explicit expressions and detailed physical interpretations are referred to Appendix A, Table A.1. Note that all the terms are localized both in space and in time; in other words, they are all four-dimensional field variables, distinguished notably from the classical formalisms in which localization is lost in at least one dimension of space–time in order to achieve scale decomposition. Processes localized in space and time are thus naturally embedded in (1) and (2).

Although the terms in (1) and (2) have the conventional names (e.g., Orlanski and Katzfey 1991; Chang 1993), they are actually distinctly different from those in traditional formalisms. The most distinct terms are Γ_A^{ϖ} and Γ_K^{ϖ}, which are the processes that we are most interested in for this study. In appendix A we will see that they both have *a Lie bracket form, and possess the property of Jacobian identity, reminiscent of the Poisson bracket in Hamiltonian dynamics; they also satisfy a detailed balance relation. Most importantly, they sum to zero over scale window* ϖ *and location n.* This conservation property, though simple to state, does not hold in previous energetic formalisms. To

distinguish it from those that may have been encountered in the literature, the above transfer is termed *canonical transfer*.

The canonical transfers (Γ_A^{ϖ} and Γ_K^{ϖ}) in (1) and (2) are very important. Particularly, the mean-to-eddy parts of them (written as $\Gamma_A^{0\to1}$ and $\Gamma_K^{0\to1}$) correspond to the two important geophysical fluid flow processes, *i.e.,* baroclinic instability and barotropic instability of the mean flow (see Liang and Robinson, 2007), though whether they are equivalent is still in dispute (e.g., Farrell, 1984; 1985; 1989; Plumb, 1983). For mnemonic reason, in the following, $\Gamma_A^{0\to1}$ and $\Gamma_K^{0\to1}$ may be referred to as, respectively, baroclinic and barotropic canonical transfers. Conversely, the eddy-to-mean parts, written as $\Gamma_{\mathrm{A}}^{1\to0}$ and $\Gamma_{\mathrm{K}}^{1\to0}$, can be used to investigate the eddy feedback processes. They respectively correspond to the baroclinic and barotropic feedback mechanisms. See Figure A1 for an illustration.

3.2 Eddy tracking and compositing

The methods used in this study also include an eddy tracking and compositing technique. Because of the migration of the eddies and the inhomogeneity of the background flow, an eddy-following approach is needed to investigate the localized interaction. Here the tracking algorithm developed by Hodges (1995) is used to fulfil this task. In practical use, the maxima of the 850-hPa relative vorticity (ξ_{850}) are chosen as the indicator of the storm center (or feature point), which forms the nodes of the storm trajectory (Hoskins and Hodges, 2002). Besides, before tracking the vorticity maxima associated with weather storms it is necessary to remove the background field, i.e., the

slowly varying, large spatial scale part of the field (Anderson et al. 2003). Here, we use the synoptic vorticity reconstructed by the MWT as the indicator. That is to say, the eddies tracked are storms in the synoptic scale window. Following previous studies, the cyclogenesis time is defined as the first time when ξ_{850} exceeds 1×10^{-5} s^{-1}. In this study, we only select the long-lived storms whose ξ_{850} remains larger than 1×10^{-5} s^{-1} for at least 4 days after their genesis. Also, only storms with a maximum ξ_{850} greater than 5×10^{-5} s^{-1} are retained for the analysis. Finally, trajectories of 2189 cold-month (from October to April) storms in the North Pacific storm-track area [20°N-70°N; 120°E-240°E] are obtained. A sample of the selected trajectories are displayed in Figure 1.

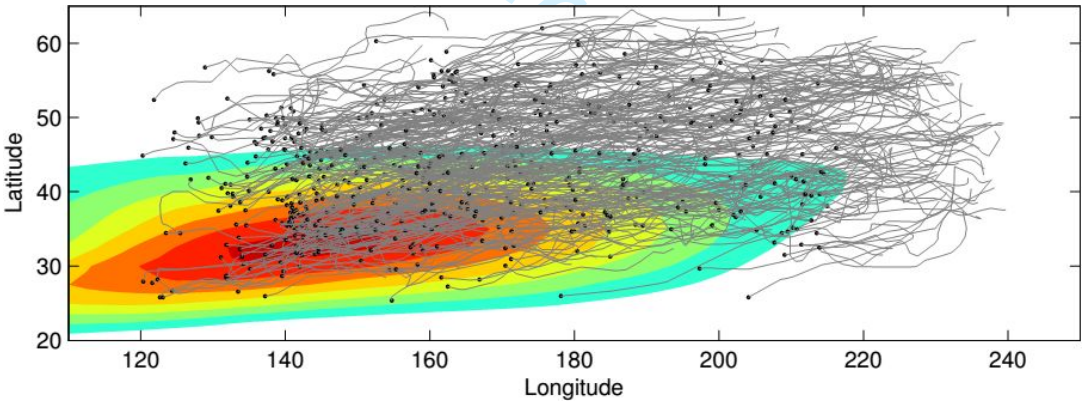

Figure 1. Sample of storm trajectories based on ξ_{850}. The gray lines stand for trajectories, with black dots indicating their respective starting points, and the shaded area for the climatological wintertime 300-hPa zonal wind, starting from 20 m s^{-1} with an interval of 5 m s^{-1}.

The cyclone trajectories obtained are used for the compositing of the spatial structures. Considering the large case-to-case variability (Sinclair and Revell, 2000), we

use the compositing method with a large number of individual storms in order to get a statistical result. A detailed description of the methodology can be found in Bengtsson et al. (2007) for a radial sampling grid since modified for a rectangular sampling grid. In brief, it consists of the following procedures:

* First, select the tracks to be used. (In the present study, the storms of interest are the 2189 long-lived strong storms.)

* Second, create a rectangular grid centered on the equator with uniform grid spacing and chosen side length (respectively 0.5 and 40 degrees here).

* Third, rotate the grid to the storm center and rotate it to align with the direction of the storm propagation, which is determined by the displacement of the storm center using a second-order, central differencing scheme. Using the rotated composite can reduce the impact of the difference in the storm propagation direction on the composite storm structure.

* Finally, the required field is sampled on to the rectangular grid, for each storm at each time step along the full lifecycle of the storms and then averaged over the selected storms at selected stages of the lifecycle. For the averaging, we need a reference time for the lifecycle. In this study, the instant of maximal intensity is chosen as t = 0, and then the time is measured as offset to this reference time. For example, -4 (4) stands for 4 time steps (or 24 h) before (after) the storm reaches its maximal intensity. In this study, the standard deviation is used to show the case-to-case variability within the composites.

4. MS-EVA setup

The analysis begins with a determination of the scale window bounds. In this study, we need two windows: a synoptic-scale window and a low-frequency background flow window. According to previous studies, these windows are set to be bounded by a period of 16 days (in MWT, the number of time steps is required to be a power of 2). We have also tried 8 days as the window bound and found that the synoptic signal cannot be completely separated from the total fields. This is essentially the same as Deng and Mak (2006), who applied a 15-day high-pass filter in their diagnostics. Besides, Anderson et al. (2003) observed that band-pass filtering with a time period of 2.5-6 days (e.g., Blackmon, 1976) may have a detrimental impact on individual weather systems (see also Chang, 1993), and a 20-day high-pass filter is a good choice.

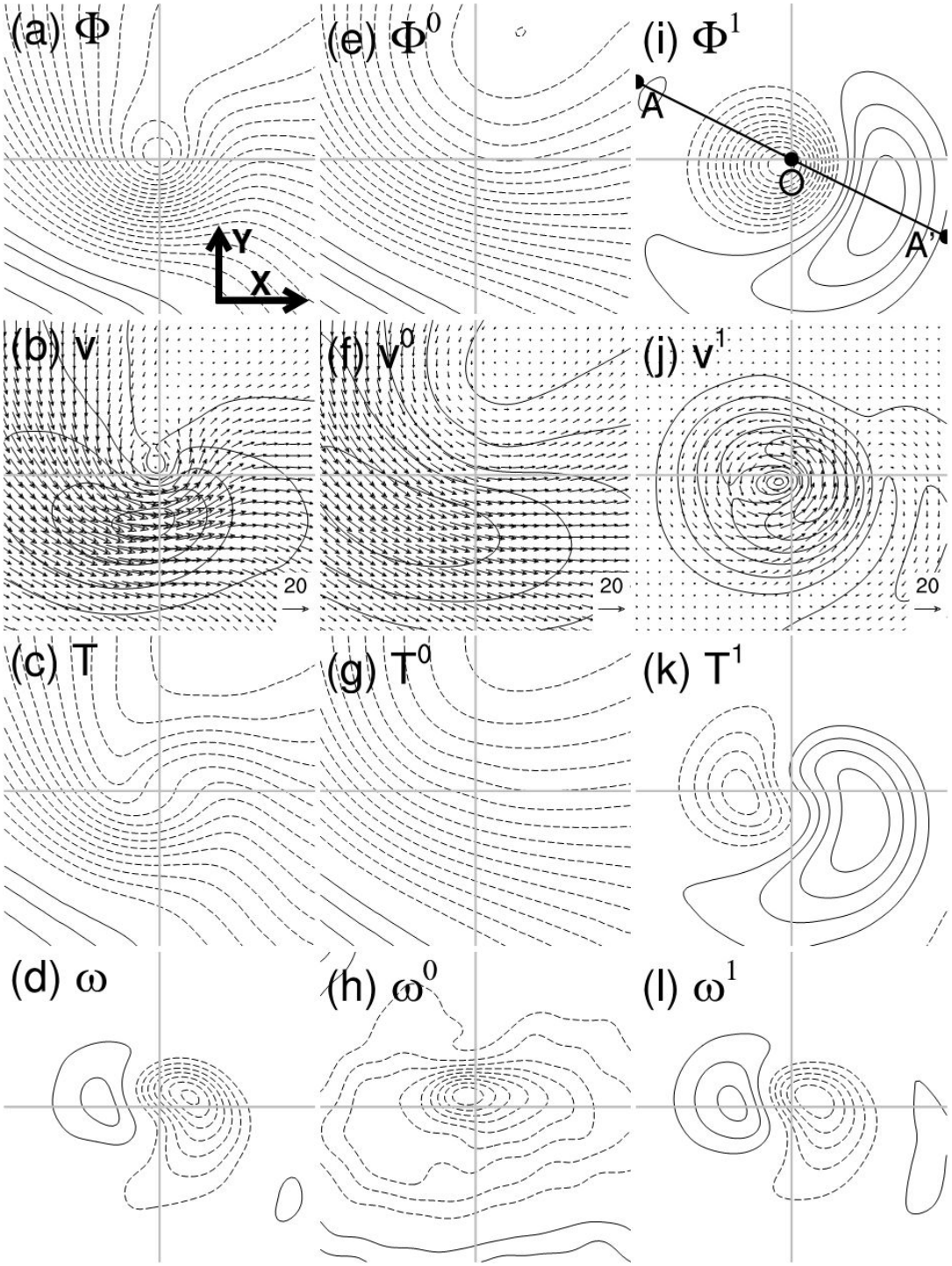

Figure 2. Left column: distributions of the 500-hPa composite original fields at the maximal intensity time (t=0): (a) geopotential anomalies (contour interval 200 $m^2 s^{-2}$), (b) wind vectors (m s^{-1}) and speeds (contour, contour interval 5 m s^{-1}), (c) temperature

anomalies (contour interval 1 K), and (d) vertical velocity (contour interval 0.04 Pa s^{-1}). **Middle column:** same as the left column, but for the background fields, with contour intervals of (e) 200 m^2 s^{-2}, (f) 3 m s^{-1}, (g) 1 K, and (h) 0.004 Pa s^{-1}. **Right column:** same as the left column, but for the synoptic fields, with contour intervals of (i) 100 m^2 s^{-2}, (j) 2 m s^{-1}, (k) 0.5 K, and (l) 0.04 Pa s^{-1}. Negative contours are dashed and the zero contour is omitted. The composite storm propagates eastward. Each subplot is in a 40° × 40° rectangular grid. The composites are based on the 2185 cold-month (October-April) storms; same below. The corresponding distributions of the standard deviation are given in Figure S3 in the supplementary file.

5. Composite structure of the original and reconstructed fields

In this section, we briefly describe the composite structures of the original and reconstructed fields. Since the structure of each composite field changes little throughout the life of the composite storm, only the maps at the storm's maximal intensity time (t = 0) are presented (note that the storm strength changes significantly throughout the life; see Figures S1 and S2 in the supplementary file). Figure 2 shows the horizontal distributions of the composite fields at 500 hPa. The side length of each subplot is 40 degrees at the equator (equivalent to 4447 km). The composite system moves from the left to the right. For convenience, the along-propagation direction will be referred to as the *x*-direction, and the *y*-direction and *z*-direction are determined through the right-hand rule, with *z* directed upward.

5.1 The original fields

We first look at the original fields. On the map of geopotential anomalies (ϕ), there is a trough with closed isopleths (Figure 2a). Correspondingly, a cyclonic circulation exists on the map of the horizontal wind ($\boldsymbol{v}_{\mathrm{h}}$, Figure 2b). The distribution of the wind speed is quite inhomogeneous around the storm center, with strong winds occurring in the south part where the contours of geopotential anomalies are dense. The composite field of temperature anomalies (T) exhibits a wave-like pattern (Figure 2c), with the temperature trough and ridge located to the west and east of the storm center, respectively. In terms of the vertical velocity (ω), it shows a dipole pattern (Figure 2d), with upward ($\omega < 0$) and downward ($\omega > 0$) motions located ahead and behind the geopotential trough, respectively; the upward motion is much stronger than the downward motion. The features of these composite fields generally agree with those in previous studies (Bengtsson et al., 2009; Catto et al., 2010; Dacre et al., 2012; Field and Wood, 2007).

5.2 The multiscale window reconstructed fields

We now look at the composites of the multiscale fields reconstructed by the MWT. To our knowledge, few studies have explored the storm structure in this way. Figures 2e-2h show the composite maps of the background fields. We see that the contours of geopotential anomalies ($\phi^{\sim 0}$) are generally northwest-southeastward distributed (Figure 2e), and the closed center appearing in the original field (Figure 2a) has been removed. The background wind maximum (i.e., the jet stream) is located in the south (Figure 2f). This is why the maximum wind occurs in the southern part of the storm on the original

map (Figure 2b). For temperature anomaly ($T^{\sim 0}$), its distribution (Figure 2g) is similar to that of $\phi^{\sim 0}$. Regarding $\omega^{\sim 0}$, it is negative within almost the whole domain (Figure 2h), implying that the storms are generated and evolve within an environment of upward motion. The magnitude of $\omega^{\sim 0}$ is about 10% of the original field (note the difference in the contour interval between them).

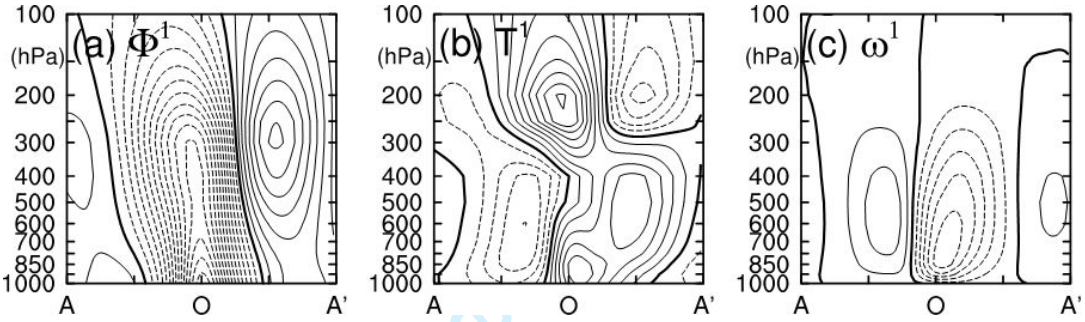

Figure 3. Vertical section distributions of the composites of the synoptic fields: (a) geopotential anomalies (contour interval 100 m^2 s^{-2}), (b) temperature anomalies (contour interval 0.5 K), and (c) vertical velocity anomalies (contour interval 0.04 Pa s^{-1}). Negative contours are dashed and the zero contour is in bold. All these sections are taken along the line (AOA') as indicated in Figure 2i. The corresponding distributions of the standard deviation are given in Figure S4 in the supplementary file.

Figures 2i-2l show the distributions of the composite synoptic fields, which exhibit more local features than the background fields. The composite field of the 500-hPa $\phi^{\sim 1}$ shows a low-high pair (Figure 2i). The low anomaly has compact structure and large amplitude, accompanying a strong cyclonic circulation (Figure 2j), whereas its counterpart is broad and weak. For the other anomaly fields ($T^{\sim 1}$ and $\omega^{\sim 1}$), generally show a dipolar pattern (Figures 2k and 2l). Their distributions are configured in the way

that the moist-warm air ascends in the front part of the storm and the dry-cold air subsides in the rear part.

The vertical structure of the composite synoptic system is also examined. Figure 3 shows the distributions of the composite synoptic fields along the section AOA' as indicated in Figure 2i. This generally exhibits the structure of typical midlatitude baroclinic waves, with a zonal wavelength of ~4000 km and a westward (eastward) tilting of the phase line of $\phi^{\sim 1}$ ($T^{\sim 1}$) with altitude (Chang, 1993; Hartmann, 1974; Lau, 1979; Lim and Wallace, 1991). However, note the strong cyclone-anticyclone asymmetry. For example, the cyclone is strongest at low levels, whereas the accompanying anticyclone achieves its maximum at upper levels with weak signal at the earth surface (Figure 3a).[1] For $\omega^{\sim 1}$, the upward motion in the front part is much stronger than the downward motion in the rear (Figure 3c).

6. Nonlinear eddy-mean flow interaction

6.1 Spatial structure of the canonical transfers

The eddy-mean flow interaction includes the canonical transfer from the mean flow to the eddies ($\Gamma_{\mathrm{A}}^{0\to 1}$ and $\Gamma_{\mathrm{K}}^{0\to 1}$) and for the opposite direction ($\Gamma_{\mathrm{A}}^{1\to 0}$ and $\Gamma_{\mathrm{K}}^{1\to 0}$). The former is a quantitative description of the mean-to-eddy transfer and the latter characterizes the eddy feedback. We first look at the spatial structure of the former.

[1] To the best of our knowledge, the splitting of the warm center (at 850 hPa) ahead of the cyclone has not been observed (Figure 3b).

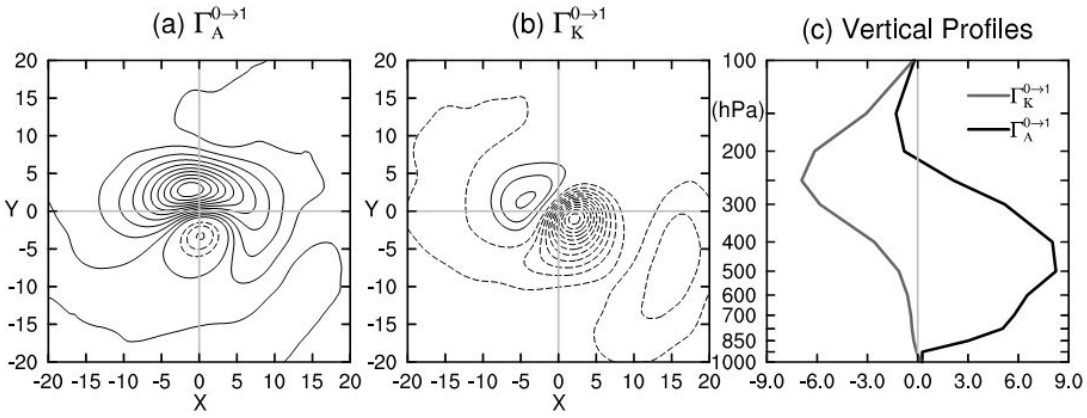

Figure 4. Horizontal distributions of the vertically integrated (from 1000 hPa to 100 hPa) (a) $\Gamma_A^{0\to1}$ and (b) $\Gamma_K^{0\to1}$ at the maximal intensity time (t=0), with a contour interval of 2×10^{-4} m^2 s^{-3}; and (c) the vertical distributions of $\Gamma_A^{0\to1}$ and $\Gamma_K^{0\to1}$ (10^{-4} m^2 s^{-3}) averaged over the storm area. The corresponding distributions of the standard deviation are given in Figure S5 in the supplementary file.

Figure 4 shows the horizontal distributions of the vertically integrated (from 1000 hPa to 100 hPa) $\Gamma_A^{0\to1}$ and $\Gamma_K^{0\to1}$. Figure 4a shows a dipolar pattern for the $\Gamma_A^{0\to1}$, with a strong positive center in the north of the storm and a weak negative center in the south. This means that the background flow experiences a downscale canonical APE transfer in the north of the storm, while an upscale canonical APE transfer in the southern region. The barotropic canonical transfer $\Gamma_K^{0\to1}$ (Figure 4b), also exhibits a dipolar distribution within the storm area, with a negative region at the front and a positive one at the rear, implying upscale and downscale canonical KE transfers in the respective regions. In terms of the amplitude the negative barotropic canonical transfer center is stronger than its positive counterpart. On the whole, the storm has a favorable configuration for APE to be transferred from the mean flow, and for KE to be transferred to the mean flow,

consistent with the traditional perspective (Barnes and Young, 1992; Orlanski and Chang, 1993; Simmons and Hoskins, 1978, 1980). Figure 4c shows the vertical profiles of $\Gamma_{\mathrm{A}}^{0\to1}$ and $\Gamma_{\mathrm{K}}^{0\to1}$ averaged horizontally over the storm area. We see that $\Gamma_{\mathrm{A}}^{0\to1}$ is positive almost throughout the entire troposphere. The maximum center occurs at 400 hPa. In contrast, $\Gamma_{\mathrm{K}}^{0\to1}$ is negative through the whole depth, implying the kinetic energy transfer is from the storm to the background flow. It is strong at upper levels and reaches its maximum magnitude at 250 hPa.

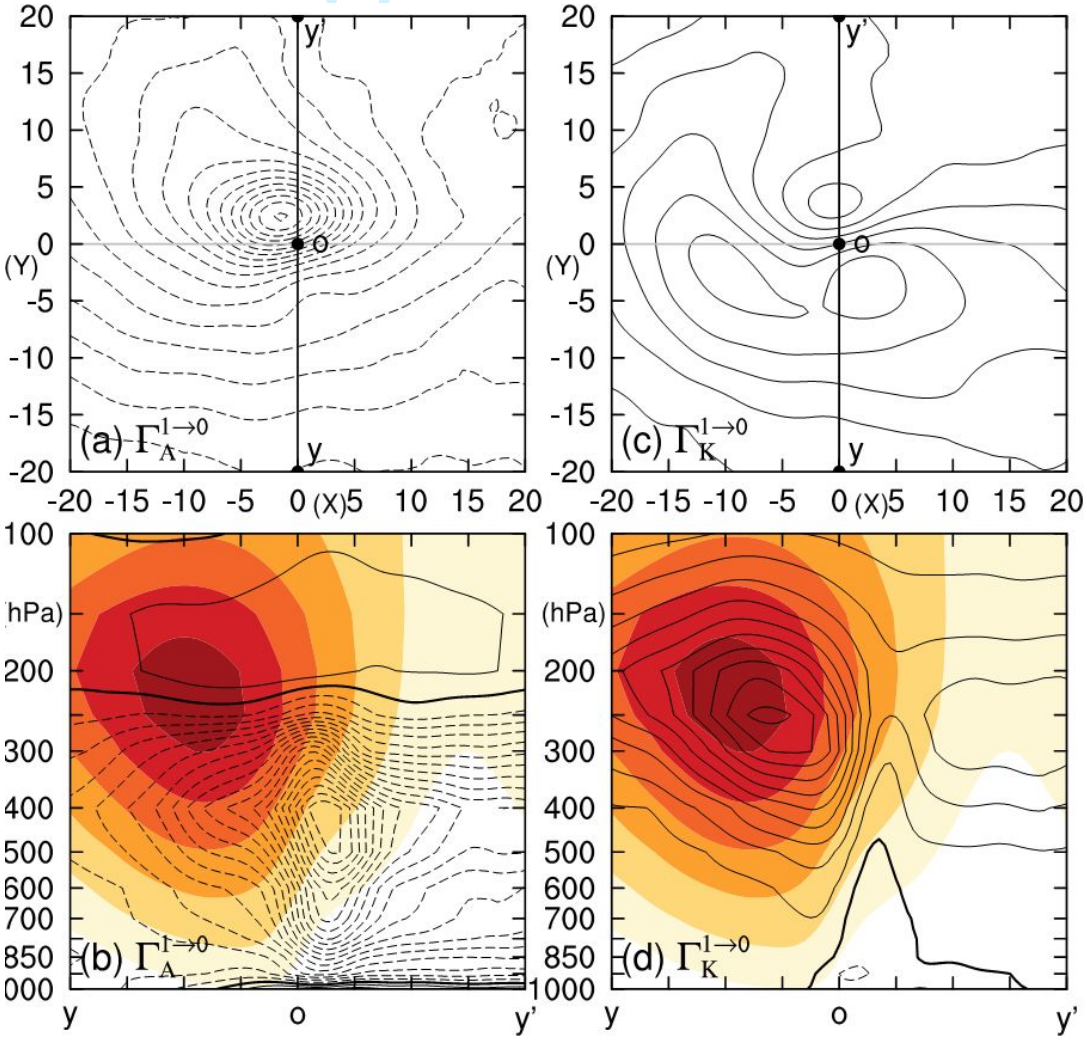

Figure 5. Spatial distributions of $\Gamma_A^{1\to0}$ and $\Gamma_K^{1\to0}$ at the maximal intensity time (t=0):

the vertically averaged (a) $\Gamma_A^{1\to0}$ and (c) $\Gamma_K^{1\to0}$; the sectional distributions of (b) $\Gamma_A^{1\to0}$ and (d) $\Gamma_K^{1\to0}$ along the line yoy' as indicated in (a) and (c). The contour interval is 0.5×10^{-4} m^2 s^{-3}. In (b) and (d), overlaid is the background wind speed $|\boldsymbol{v}^{\sim0}|$ (shaded; contour interval 4 m s^{-1}). The corresponding distributions of the standard deviation are given in Figure S6 in the supplementary file.

The spatial distributions of the eddy feedback, characterized by $\Gamma_A^{1\to0}$ and $\Gamma_K^{1\to0}$, are shown in Figure 5. We see that horizontally $\Gamma_A^{1\to0}$ is negative within the entire domain (Figure 5a), implying a downscale canonical APE transfer. But, the transfer is inhomogenous within the composite storm, with strong energy transfer mainly confined in the northern area. Vertically, $\Gamma_A^{1\to0}$ is negative through almost the entire troposphere (Figure 5b). The peak occurs at 400 hPa and on the northern flank of the jet (also the storm center). In short, the spatial distribution of $\Gamma_A^{1\to0}$ is similar to that of $\Gamma_A^{0\to1}$. For $\Gamma_K^{1\to0}$, it is generally positive (Figure 5c), implying an upscale KE canonical transfer. Note that this upscale transfer is significant at upper levels, especially at the jet core (Figure 5d). Figure 6 gives the vertical profiles of $\Gamma_A^{1\to0}$ and $\Gamma_A^{1\to0}$. It can be seen that their distributions are almost the same as the mean-to-eddy counterparts (Figure 4c), but with the opposite sign.

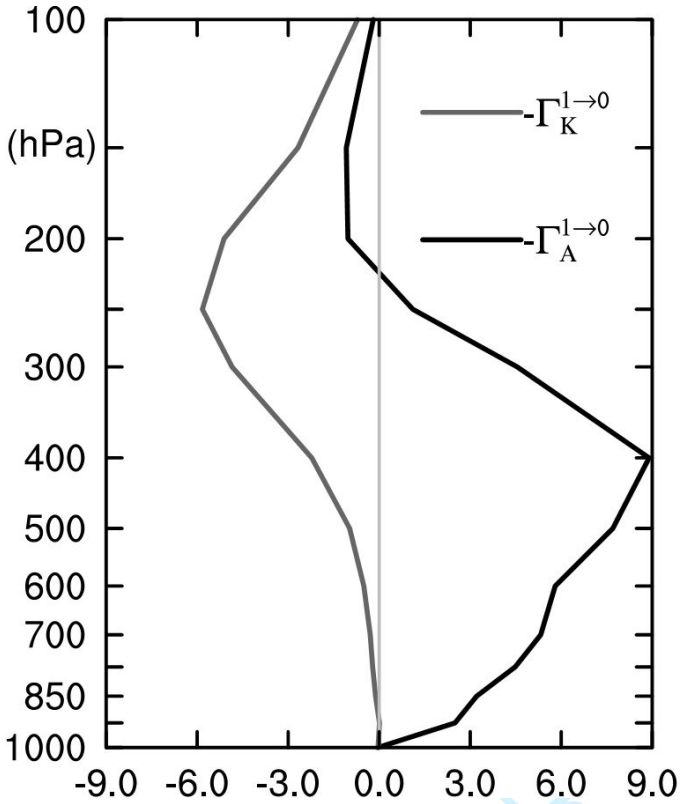

Figure 6. The vertical distributions of $-\Gamma_A^{1\to0}$ and $-\Gamma_K^{1\to0}$ (10^{-4} m^2 s^{-3}) averaged over the storm area.

6.2 Time evolution

The nonlinear eddy-mean flow interaction is not steady. Here, we are more interested in how the eddy-feedback process evolves where there is a storm passing through. To show this for a particular storm, we first identify the central location of the storm at its maximum intensity time (t=0), and then sample the vertical cross section of the fields (here $\Gamma_A^{1\to0}$ and $\Gamma_K^{1\to0}$) at that location meridionally at each time step from -12 to 12 (corresponding to from day -3 to day 3)[1]. In sampling, the fields at each time step

[1] Here we choose a duration of 6 days, considering that the mean life cycle of the 2189 storms lasts 5.37($\pm$ 0.03) days.

are also rotated with respect to the storm propagation direction at t=0. Following this way, we can get the latitude-time section of any field at a particular location as a storm approaches, passes, and recedes[1]. This procedure is applied to each of the 2189 selected storms. Finally, the obtained sections are averaged over all the samples at each time step.

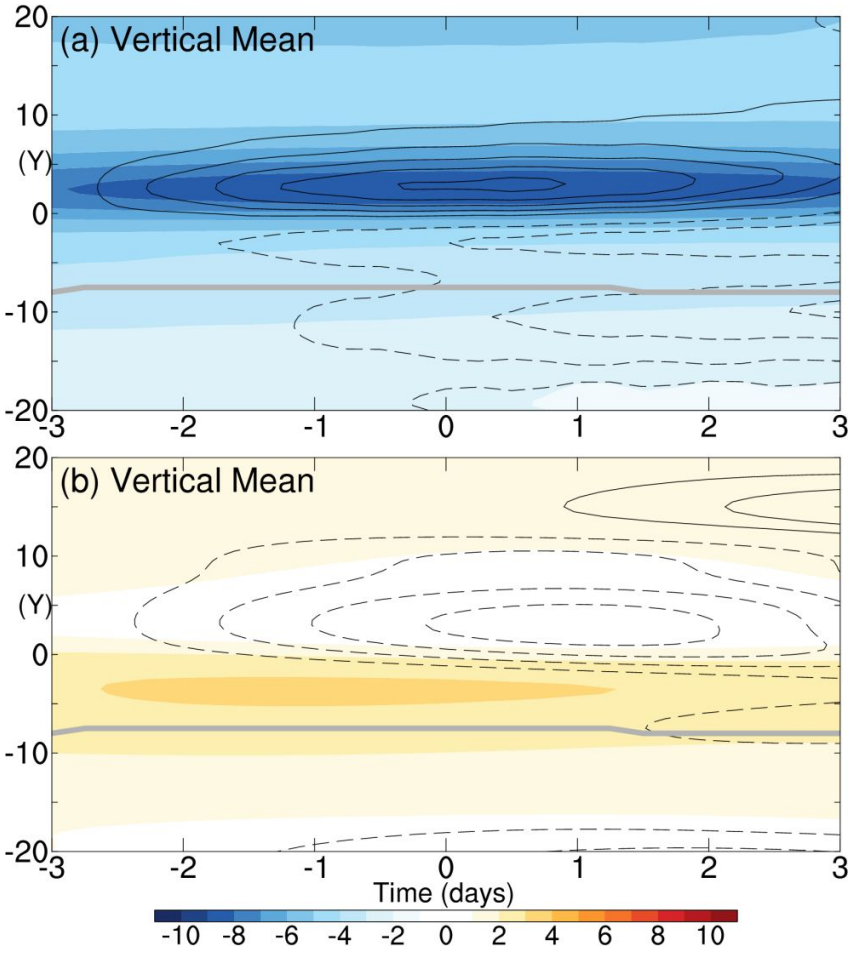

Figure 7. Vertically averaged latitude-time sections of the composite $\Gamma_A^{1\to0}$ (a; 10^{-4} m^2 s^{-3}) and $\Gamma_K^{1\to0}$ (b; 10^{-4} m^2 s^{-3}). The contours show the changes in magnitude relative to the initial state (at day -3), which are calculated as $A' = |A| - |A_*|$, with A the original

[1] Here we switch to the Eulerian approach in order to obtain the spatio-temporal distribution of the interaction and, particularly, the background flow response (see below).

field and A_* the field at day -3[1]. The contour interval is 0.2×10^{-4} m^{-2} s^{-3}. The thick gray curve in (a) and (b) denotes the latitude where the 300-hPa background wind is maximized (i.e., jet axis). The corresponding distributions of the standard deviation are given in Figure S7 in the supplementary file.

Figure 7 shows the general time evolution of $\Gamma_{\mathrm{A}}^{1\to0}$ and $\Gamma_{\mathrm{K}}^{1\to0}$. We see that as the storm passes, the downscale APE transfer is intensified within a narrow zonal band north of the storm center, whereas elsewhere it is slightly weakened (Figure 7a). In contrast, the upscale KE transfer is intensified slightly within a narrow zonal band on the southern side, while in the north it is greatly weakened (Figure 7b). The changes of $\Gamma_{\mathrm{A}}^{1\to0}$ and $\Gamma_{\mathrm{K}}^{1\to0}$ begin from about 3 days before the storm arrives, achieve their maxima as the storm arrives, and then weaken. In the presence of the storm, $\Gamma_{\mathrm{A}}^{1\to0}$ and $\Gamma_{\mathrm{K}}^{1\to0}$ seem to take place complementarily in the horizontal plane: $\Gamma_{\mathrm{K}}^{1\to0}$ intensifies (weakens) wherever $\Gamma_{\mathrm{A}}^{1\to0}$ substantially weakens (intensifies).

The most interesting finding in this section is the spatial asymmetry of the eddy-mean flow interaction: the downscale canonical APE transfer process mainly happens in the northern part of the storm (also on the northern flank of the jet stream) and in middle levels, whereas the upscale canonical KE transfer mainly occurs in the south, overlaid with the jet core. The former acts to destroy the background baroclinicity, whereas the latter acts to accelerate the jet and thus enhance the baroclinicity. These

[1] Here we want to see the change in energy transfer as a storm arrives but initially there is no storm, so we choose an earlier day (i.e., day -3) rather than day 0.

competing effects essentially determine the final state of the jet stream after the storm passes. We will elaborate on this in the following section.

7. Response of the background flow and baroclinicity

In this study, we focus on the responses of the background wind and baroclinicity. Figure 8 shows the composite sections of the background wind (left column). We see that as the storm passes, the wind decreases in the north, whereas it increases in the south, showing an anomalous dipolar pattern (Figure 8a). Moreover, the increase in the south is stronger than the decrease in the north. Since the jet core is located in the south of the storm (cf. Figure 3), this tends to strengthen and narrow the jet (by 2 latitudes)[1]. Figures 8c and 8d show the composite pressure-time sections of the background wind along the latitudes of 10° and -10°, respectively. It can be seen that either in the north or in the south, the response of the background wind is more significant in the upper troposphere (Figures 8b and 8c). Temporally, the background wind begins to change from about 3 days before the storm's arrival, and responds strongly as the storm arrives. A closer observation reveals that the largest change occurs at t=2d instead of t=0 (see also the energy transfers in Figure 7). This may be due to the consecutive influence of secondary cyclones formed along the trailing cold front of the reference one (e.g., Papritz and Schemm 2013). Overall, the jet does not show any obvious meridional shift. This is consistent with the argument of Vallis and Gerber (2008) that, if the storm is generated

[1] This estimation is based on the half jet-width, which is measured by the distance between the latitude of maximum wind and the northward latitude at which the wind reaches half of its peak.

on the flank of the jet, the storm would act to maintain the jet's latitude. For the background wind response at any instant (e.g., t=0), the meridional structure is similar to that obtained by Chang (2001b) using wave packet regression.

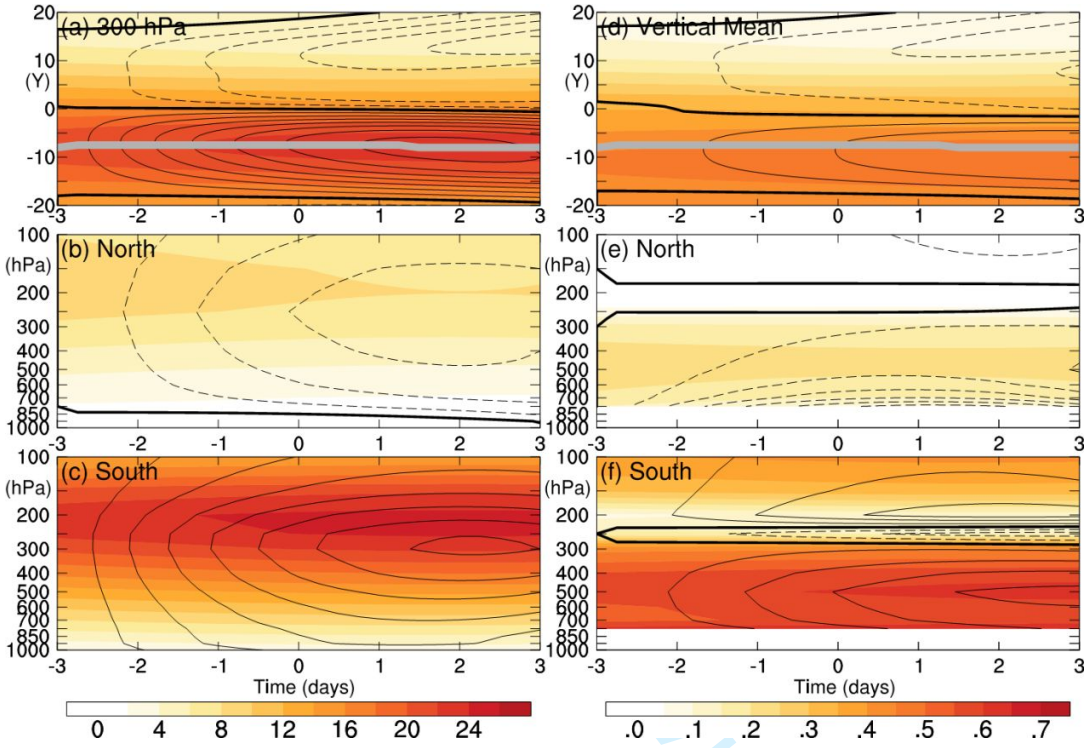

Figure 8. Left column: same as Figure 7, but for the background wind speed (shaded, m s^{-1}) and its anomaly (contoured, with an interval of 0.25 m s^{-1}); (a) shows the latitude-time section at 300 hPa; (b) and (c) show the pressure-time sections along the latitudes of 10° and -10°, respectively. The thick gray curve in (a) and (d) denotes the latitude of the maximum of the 300-hPa background wind. Right column: same as the left column, but for the baroclinicty, i.e., the Eady growth rate (shaded; in day^{-1}) and its anomaly (contoured, with an interval of 0.01 day^{-1}). The corresponding distributions of the standard deviation are given in Figure S8 in the supplementary file.

The latitude-time section of the baroclinicity, measured by $fN^{-1}|\partial\bar{v}/\partial z|$ (where N is the static stability and other symbols are conventional), is also shown in Figure 8 (right column). We see that, as the storm passes, the baroclinicity weakens in the north, whereas it strengthens in the south (Figure 8d). Vertically, the largest northern weakening happens in the lower troposphere (Figure 8e), while the strongest southern strengthening occurs at middle levels (Figure 8f).

There is a discrepancy between the evolution of the energy transfers and that of the background flow. Figure 7 suggests that the downscale transfer north of the cyclone is much stronger than the upscale transfer south of the cyclone, while Figure 8 show that the jet/baroclinicity decrease north of the cyclone is somewhat smaller than the jet/baroclinic increase south of the cyclone. How does this discrepancy happen? In fact, the energy transfer is not the only factor that can cause change in the background field. In addition to the nonlinear interaction process, many other energy processes (e.g., energy flux convergences) are also involved, and they can redistribute the energy in horizontal space (Papritz and Schemm 2013; Rivière et al. 2015). Figure 9 shows the mean distribution of the horizontal kinetic energy flux convergence along the meridional direction. It can be seen that the convergence is strong on the southern side of the storm center and peaks near the jet center. Moreover, the convergence is mainly due to the zonal component of the KE flux (Figure 9b). This indicates that, apart from the energy transfer, nonlocal processes also play a role in the enhancement of the background flow in the southern side of the storm.

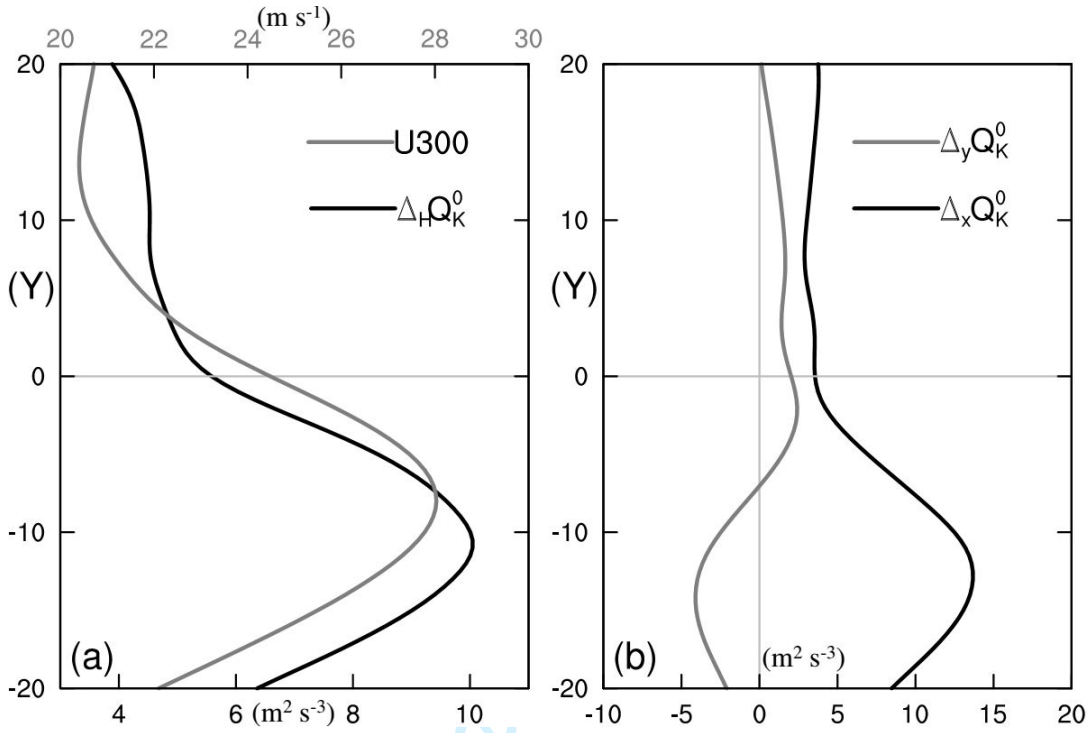

Figure 9. (a) Mean distributions of the horizontal kinetic energy flux convergence (in black; 10^{-4} m^2 s^{-3}) and 300-hPa wind speed (in gray; m s^{-1}) versus *y*; (b) same as (a), but for the x- and y-components of the kinetic energy flux convergence.

8. Discussion

In the above we have discussed about the average results of all the 2189 storms, and overall the composite storm is located on the northern side of the maximum background wind speed (refer to Figures 2, 5, etc.). But if we have a closer look at these storms, actually four types of relative locations can be classified.

In order to determine the relative location of a storm, we sample the 300-hPa zonal wind in equal-distance along the meridian passing through the storm center. We take the center as the starting point (0°) and sample the wind speed once every 2.5° to the south and north, respectively. The sampling range is from -20° (south) to 20° (north). Based on

the resulting meridional profile of the background zonal wind, the relative location is then determined. We first calculate the average meridional gradient of zonal wind north and south of the storm center, which here is simply represented by the difference $\Delta = \overline{u_{i+1} - u_i}$ (the overbar stands for meridional average). For convenience, the average gradient on the southern side and the northern side are referred to as Δ_S and Δ_N, respectively. If $\Delta_S < 0$ and $\Delta_N < 0$, it means that the storm center is located on the northern side of the jet, and we call this type of configuration Type-1; if $\Delta_S > 0$ and $\Delta_N > 0$, the storm center is located on the southern side of the jet, and we call this configuration Type-2; if $\Delta_S > 0$ and $\Delta_N < 0$, the storm is at the center of the jet, and the configuration is classified as Type-3; if $\Delta_S < 0$ and $\Delta_N > 0$, it means that there are two jets, and the storm lies in between---we call this configuration Type-4.

By the above classification it is found that there are 909 Type-1, 93 Type-2, 881 Type-3, and 299 Type-4 configurations, plus 7 cases belonging to nowhere. The mean meridional profiles of the background zonal wind corresponding to these four configuration types are shown in Figure 10. It can be seen that if only the configuration between the storm and the major jet is considered, the Type-4 case is similar to the Type-1 case, i.e., the configuration with storms located on the northern side of the major jet. The result is, the Type-1 and the Type-4 storms together account for 55.2% of the total 2189 storms, consistent with the previous observation that the storm track is generally located on the poleward flank of the jet (e.g., Blackmon et al., 1977; Chang et al., 2002). On the other hand, the Type-3 storms are not exactly located at the center of

the jet, but northward of it by 2.5°. Despite being a minority, 93 storms appear southern side of the jet. One may wonder whether these four kinds of storms have different interaction scenarios from each other. In the following, we discuss these four types of storms separately and compare and contrast them.

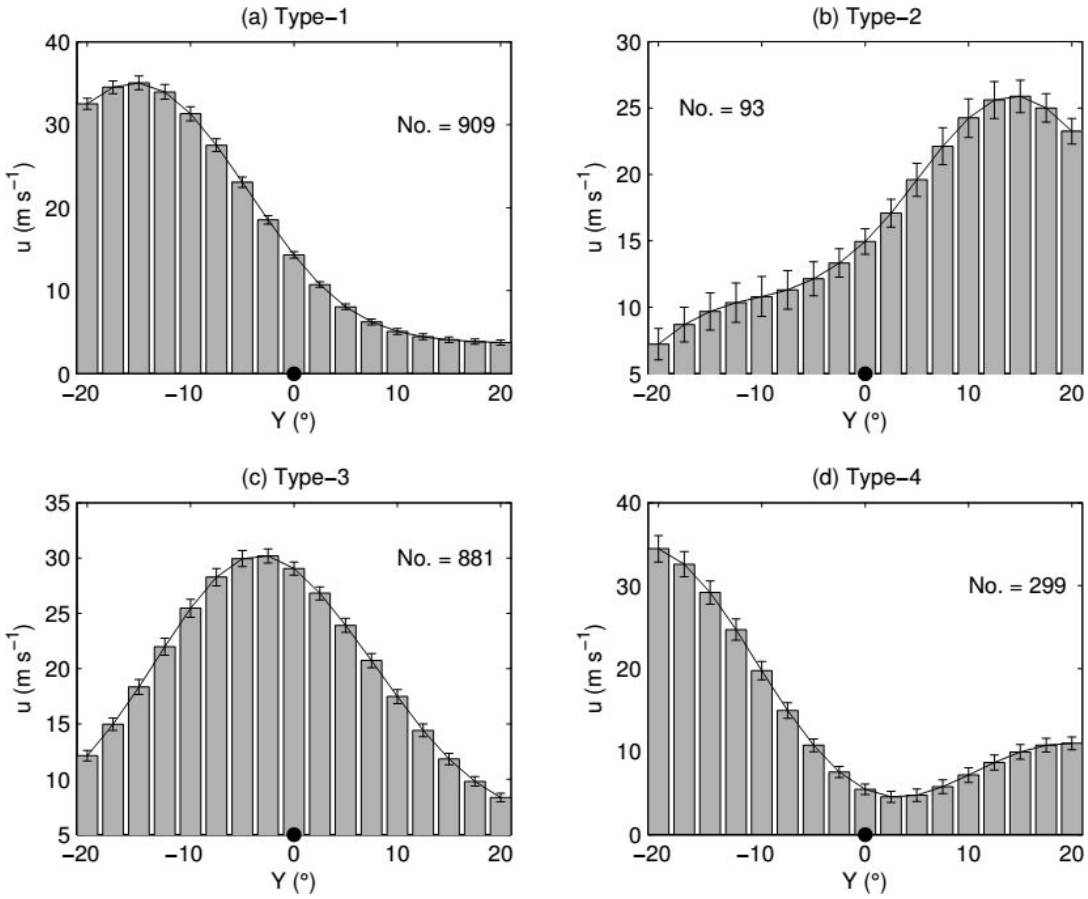

Figure 10. The four types of zonal wind profiles. (a) Type-1: the storm is on the northern side of the jet; (b) Type-2: the storm is on the southern side of the jet; (c) Type-3: the storm is at the jet center; and (d) Type-4: the storm is located between two jets. The black dot indicates the meridional location of the storm center. The error bars represent the uncertainties of the mean at the 5% significance level.

Figure 11 shows the distribution of the composite 500-hPa geopotential anomalies

for the four types of storms. As expected, the distributions of the Type-1 and Type-4 storms are similar since both of them are located on the northern flank of the jet. Besides, their distributions (Figures 11a-c, 11j-l) are similar to the general results as shown in Figures 2a, 2e, and 2i, with a wide trough in the background field (Figures 11b, k) and a dipole in the synoptic field (Figures 11c, l). This is easy to understand because these two types together account for the largest proportion of the total storms. Although the Type-3 storm is located near the jet center, the distribution of its geopotential anomalies (Figures 11g-i) is still similar to those of Type 1 and Type 4. The obvious difference lies in the Type-2 storm. There is a distinct anti-cyclonic circulation on the southern side of the storm in the original field (Figure 11d), which is not seen in the other three types. In addition, it can be found that the propagation direction of the Type-2 storm is basically parallel to the isolines of the background geopotential (Figure 11e), whereas that of the other three types intersects the isolines and points to the left side.

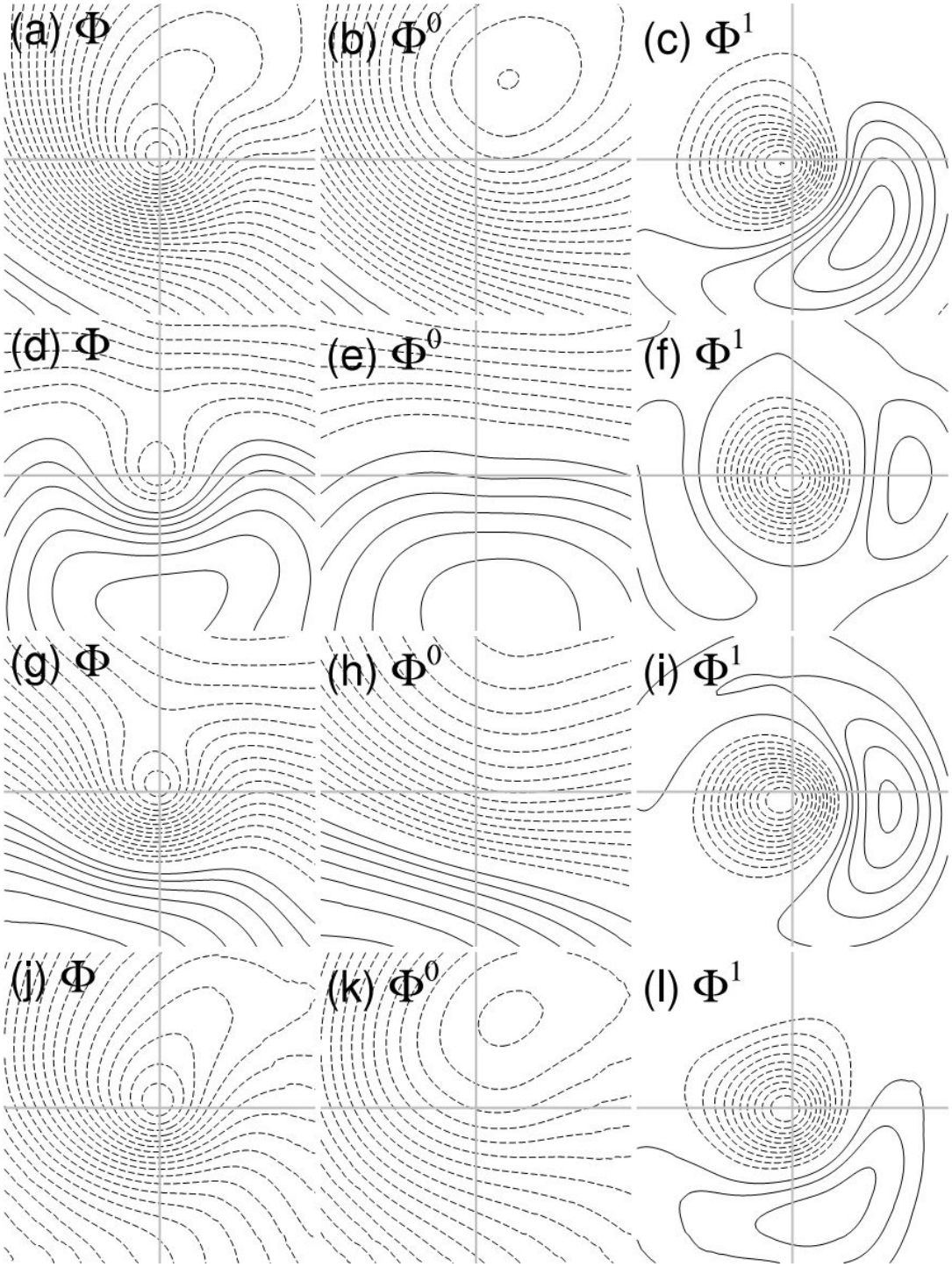

Figure 11. Same as Figures 2a, 2e, and 2i, but for the Type-1 storm (a, b, c), Type-2 storm (d, e, f), Type-3 storm (g, h, i), and Type-4 storm (j, k, l), respectively. The corresponding distributions of the standard deviations are displayed in Figure S9 in the

supplementary file.

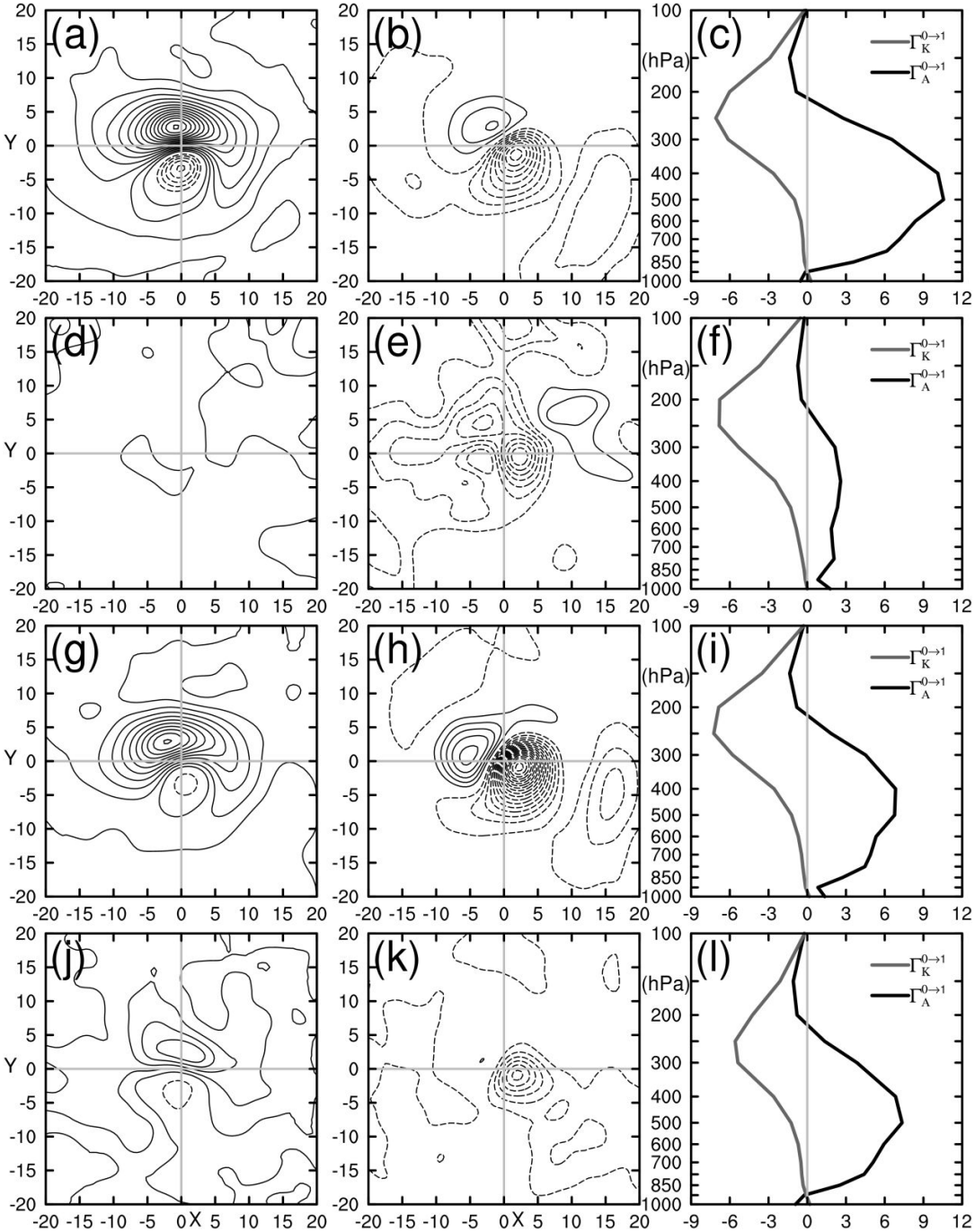

Figure 12. Same as Figure 4, but for the Type-1 storm (a, b, c), Type-2 storm (d, e, f), Type-3 storm (g, h, i), and Type-4 storm (j, k, l), respectively. Left column: $\Gamma_A^{0\to1}$; Middle column: $\Gamma_K^{0\to1}$. The corresponding distributions of the standard deviations are

given in Figure S10 in the supplementary file.

The horizontal distributions of the vertically integrated canonical transfers $\Gamma_A^{0\to1}$ and $\Gamma_K^{0\to1}$ are given in Figure 12. It can be seen that the Type-1 (Figures 12a, b), Type-3 (Figures 12g, h), and Type-4 (Figures 12j, k) storms generally bear the same structure, similar to the general results as shown in Figure 4. For instance, $\Gamma_A^{0\to1}$ shows a dipolar pattern, with a strong positive center in the north of the storm and a weak negative center in the south. $\Gamma_K^{0\to1}$ also exhibits a dipolar distribution within the storm area, with a negative center at the front and a positive one in the rear (note the positive $\Gamma_K^{0\to1}$ center in the Type-4 storm is not obvious). In contrast, the Type-2 storm is quite different. Horizontally, $\Gamma_A^{0\to1}$ is mainly distributed in the northeast corner with small values (Figure 12d), and there is no dipole pattern as observed in the other three types. $\Gamma_K^{0\to1}$ does not show the dipolar structure, either (Figure 12e); it is negative throughout the domain, with two minima around the storm center.

Also presented in Figure 12 are the average vertical distributions of $\Gamma_A^{0\to1}$ and $\Gamma_K^{0\to1}$. The Type-1 (Figure 12c), Type-3 (Figure 12i) and Type-4 (Figure 12l) storms have the largest amplitude of $\Gamma_A^{0\to1}$ ($\Gamma_K^{0\to1}$) at middle (high) levels, similar to the general results previously revealed in Figure 4c. For the Type-2 storm, its $\Gamma_K^{0\to1}$ profile is also similar, but its $\Gamma_A^{0\to1}$ profile is quite different. Although it is still positive through most of the troposphere, it is quite weak; refer to Table 1 for a quantitative comparison.

Table 1 The average $\Gamma_A^{0\to1}$ and $\Gamma_K^{0\to1}$ for the four types of storms and the corresponding absolute ratio $\left|\Gamma_A^{0\to1}/\Gamma_K^{0\to1}\right|$.

	Type-1	Type-2	Type-3	Type-4
$\Gamma_A^{0\to1}$ (10^{-4} m^2 s^{-3})	5.3	1.5	3.7	3.5
$\Gamma_K^{0\to1}$ (10^{-4} m^2 s^{-3})	-1.9	-2.1	-2.1	-1.7
$\left\|\Gamma_A^{0\to1}/\Gamma_K^{0\to1}\right\|$	2.7	0.7	1.8	2.0

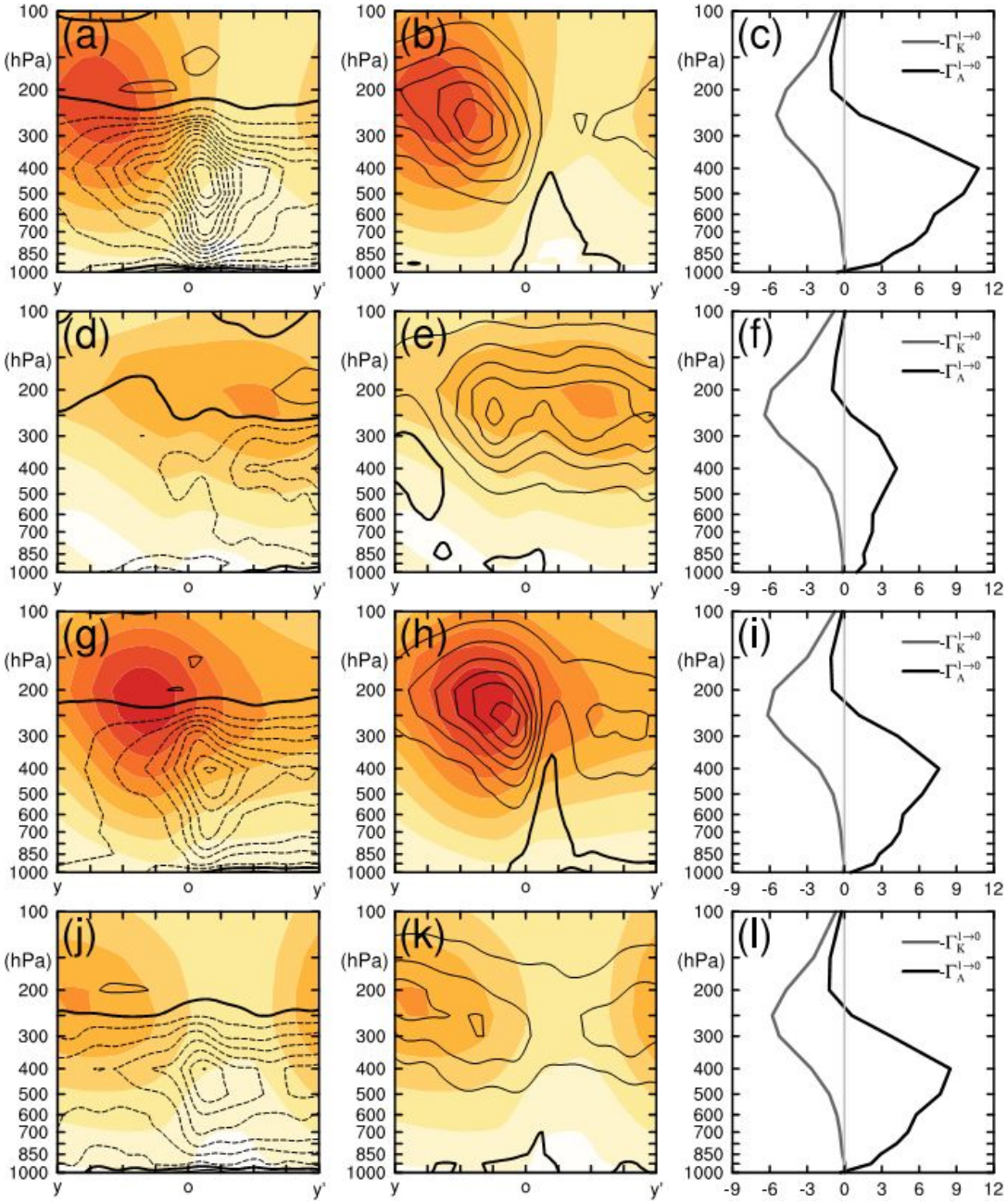

Figure 13. Same as Figures 5 and 6, but for the Type-1 storm (a, b, c), Type-2 storm (d, e, f), Type-3 storm (g, h, i), and Type-4 storm (j, k, l), respectively. Left column: $\Gamma_A^{1\to0}$; Middle column: $\Gamma_K^{1\to0}$. The corresponding distributions of the standard deviations are given in Figure S11 in the supplementary file.

Figure 13 gives the distributions of $\Gamma_A^{1\to0}$ and $\Gamma_K^{1\to0}$ over the meridional section

through the storm center. For $\Gamma_A^{1\to0}$, there is always an active center on the northern side of the Type-1 (Figure 13a), Type-3 (Figure 13g), and Type-4 (Figure 13j) storms (also the jets), whereas it is lacked in the Type-2 storm (Figure 13d). For $\Gamma_K^{1\to0}$, its center generally coincides with the jet stream. In addition, $\Gamma_K^{1\to0}$ seems to be enhanced in the southern part of the storm. For instance, the $\Gamma_K^{1\to0}$ maximum always occurs there, although the jet sometime is located in the north (see Figure 13e). Vertically, the distributions of $\Gamma_A^{1\to0}$ and $\Gamma_K^{1\to0}$ (Figures 13c, f, i, l) are basically the same as the mean-to-eddy counterparts (Figures 12c, f, i, l), but with the opposite sign.

The time evolution of the vertically averaged $\Gamma_A^{1\to0}$ and $\Gamma_K^{1\to0}$ is given in Figure 14. Generally, the evolutions of Type 1, Type 3, and Type 4 are similar, with $\Gamma_A^{1\to0}$ ($\Gamma_K^{1\to0}$) strengthened in the north (south) of the storm and weakened in the south (north). In contrast, Type 2 is different. Its $\Gamma_A^{1\to0}$ is strengthened near the storm center and is weakened in the south and north (Figure 14c), whereas the $\Gamma_K^{1\to0}$ changes in the opposite direction (Figure 14d).

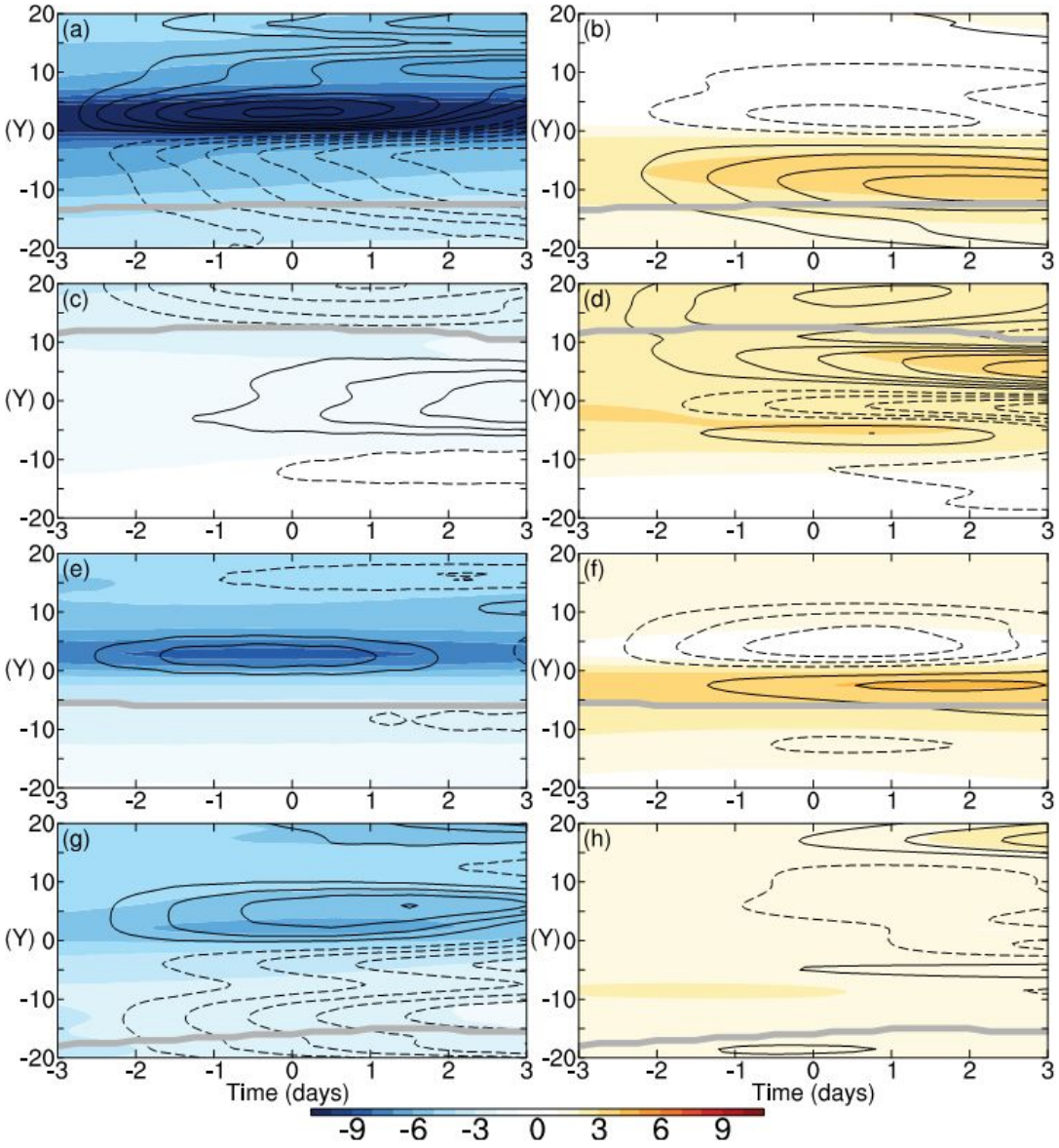

Figure 14. Same as Figs. 7a and 7b, but for the Type-1 storm (a, b), Type-2 storm (c, d), Type-3 storm (e, f), and Type-4 storm (g, h). Left column: $\Gamma_{\mathrm{A}}^{1\to0}$; right column: $\Gamma_{\mathrm{K}}^{1\to0}$. The thick gray curve denotes the latitude of the maximum of the 300-hPa background wind. The corresponding distributions of the standard deviations are given in Figure S12 in the supplementary file.

To show the response of the background wind, displayed in Figure 15 is the time

evolution of the background wind speed at the lower and upper tropospheric levels. Under the influence of the storm (of any type), the background wind speed is weakened in the north of the storm and is strengthened in the south, showing an anomalous dipolar distribution. Besides, the background wind response basically shows an equivalent barotropic structure in the vertical direction, and the response is most prominent at upper levels. It is worth noting that the Type-1, Type-3, and Type-4 storms are located near and to the north of the jet center, thus accelerating the jet, whereas the Type-2 storm is located on the south side of the jet center, weakening the jet. In addition, the wind response to the Type-2 storm is more complex than the other three types (see Figures 15c, d). In general, the response of the background wind speed is consistent with that of the canonical transfers, except for Type 2, implying that other processes may also play a role for this type of storms (refer to sec. 7).

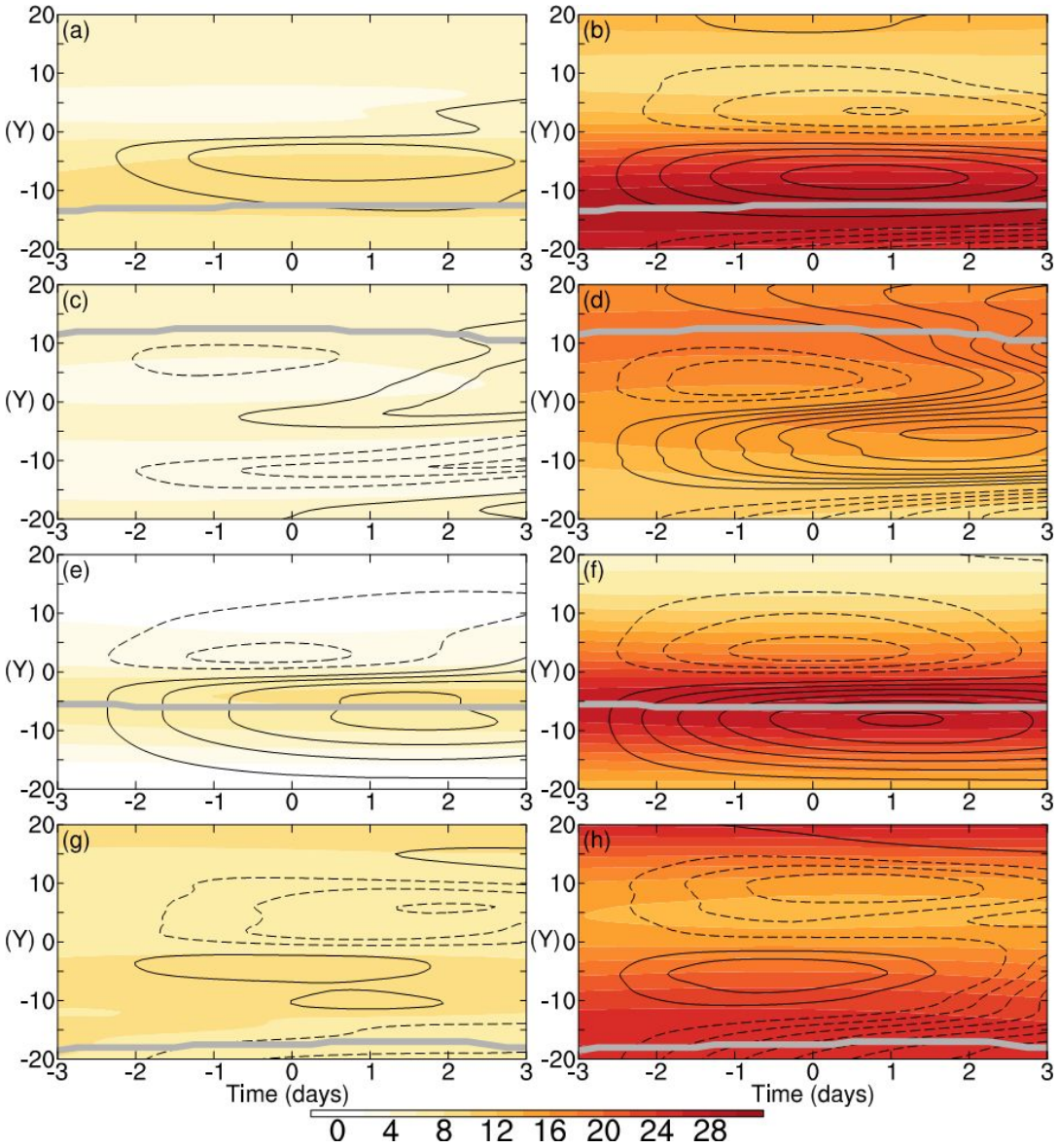

Figure 15. Same as Fig. 8a, but for the Type-1 storm (a, b), Type-2 storm (c, d), Type-3 storm (e, f), and Type-4 storm (g, h), respectively. Left column: 850 hPa; Right column: 300 hPa. The thick gray curve denotes the latitude of the maximum of the 300-hPa background wind. The corresponding distributions of the standard deviations are given in Figure S13 in the supplementary file.

To summarize, all the four types of storms basically exhibit a north-south

asymmetry in the interaction with the background flow, especially when the storm appears near or to the north of the jet center. When the storm lies to the south of the jet, the baroclinic canonical transfer turns out to be weak and its overall transfer is also weakened, quite different from the other three types. The response of the background wind field to the four types of storms generally exhibits a north-south oriented dipolar distribution, with positive anomaly in the south and negative anomaly in the north. But the Type-1, Type-3, and Type-4 storms strengthen the jet stream[1], whereas the Type-2 storm weakens the jet stream.

In a word, the interaction and background wind response for the Type-1, Type-3, and Type-4 storms are essentially similar to what we have obtained previously with all the storms considered together. The discrepancy is with the Type-2 storm. However, it should be noted that here the sample for this type is too small (with only 93 members). Its contribution is hence relatively limited and, besides, the reliability of the result also needs to be further verified.

[1] For the Type-4 storm, the strengthening of the background wind at upper level happens on the northern flank of the jet.

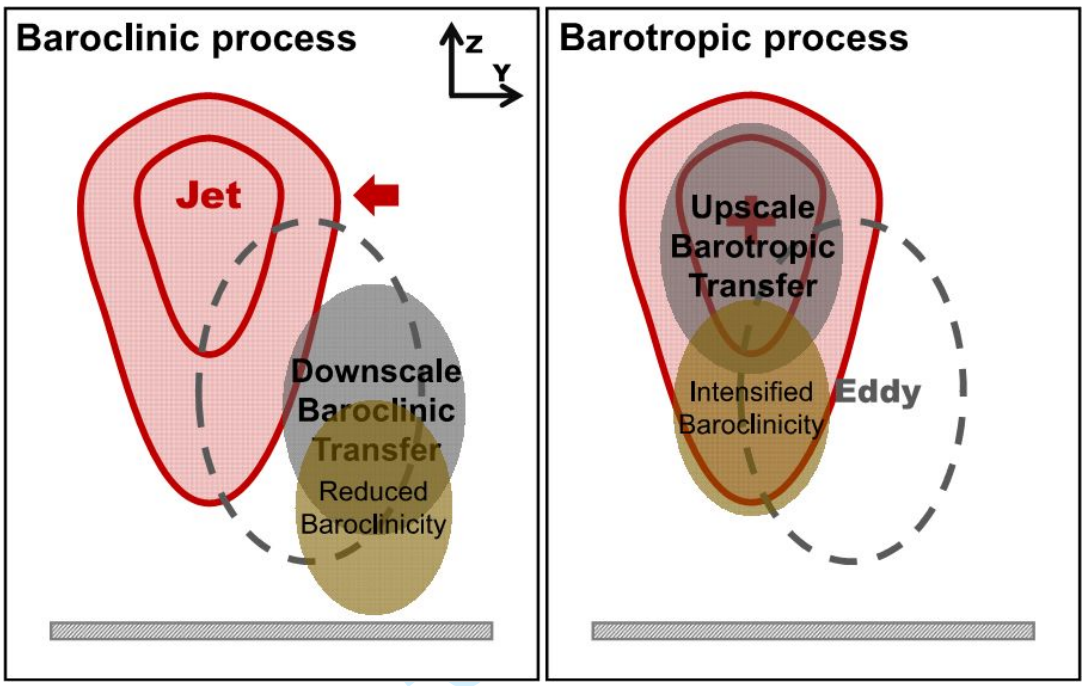

Figure 16. Schematic of the typical eddy feedback in the North Pacific storm track: (left) the bacroclinic processes, and (right) the barotropic processes. Red and dashed gray contours denote the jet and the synoptic eddy, respectively. The gray shaded area stands for the canonical energy transfer centers, and the yellow shaded area are that with baroclinicity change. The arrow in the left panel indicates the shrinking of the jet, and the plus sign in the right panel indicates the jet acceleration.

9. Conclusions

Using a recently developed methodology, namely, the Multiscale Window Transform (MWT) and the MWT-based localized multiscale energetics analysis and vorticity analysis (MS-EVA), and an eddy tracking and compositing technique, this study investigates the general structure of the nonlinear interaction between the individual synoptic eddies and the jet stream over the North Pacific storm track, based on the

ERA40 reanalysis data from ECWMF.

It is found that in the North Pacific storm track, more than 50% (Type 1 and Type 4) of the storms happen on the northern flank of the jet, about 40% are near the jet center, with very few occurring south of the jet (less than 5%). For the latter, the baroclinic canonical transfer is rather weak. For the former two types of storms (near or to the north of the jet center), their interaction with the background flow is quite asymmetric in space. Specifically, the storms experience in the north a strong downscale canonical transfer of APE, which weakens the baroclinicity and the background wind, while in the south, a strong upscale canonical transfer of KE happens at the jet core which accelerates the jet and enhances the baroclinicity. The resultant effect is that the jet strengthens but narrows, resulting in an anomalous dipolar pattern in the background wind and baroclinicity field. The general interaction scenario is schematized in Figure 16. (Note that the response of the jet may also be partially due to other processes such as large scale energy fluxes.) On average, the local interaction begins from about 3 days before a storm arrives at the site of observation, achieves its maximum as the storm arrives, and then weakens.

In this study, the eddy-mean flow interaction has been investigated within the whole north Pacific storm track throughout the entire cold season (October-April) without considering the spatiotemporal variability, which is worth further investigation. As we know, the strength and latitudinal location of the jet change remarkably with time throughout the year (e.g., the jet is strong and located more equatorward in winter whereas weak and located more poleward in summer). Changes in the jet's strength and

latitudinal location may lead to different eddy-mean flow interactions (Chang, 2001a; Harnik and Chang, 2004; Nakamura, 1992; Penny et al., 2013; Zhao and Liang, 2018). Besides, the eddy-mean flow interaction in the Atlantic sector may have a different scenario, which is for sure worth investigating. Previous studies have shown that the Pacific jet is more subtropical (Lee and Kim, 2003) whereas the Atlantic jet is largely eddy driven (Woollings et al., 2010). Both the Atlantic jet and storm track are more southwest-northeast titled than their counterparts over the Pacific. Moreover, it has been shown (Franzke et al., 2011; Novak et al., 2015; Woollings et al., 2010) that the wintertime North Atlantic jet exhibits significant latitudinal variability, with evidence of three preferred latitudinal locations: south, middle, and north; the corresponding storm-track characteristics may be quite different, suggesting a probably more complex eddy-mean flow interaction pattern in the Atlantic sector. We will explore these problems in our next-step studies.

Appendix A. A brief introduction of multiscale window transform, canonical transfer, and local Lorenz cycle

In this appendix, we present the needed mathematical formulas for the analysis. A detailed introduction of the methodologies is beyond the scope here; for that purpose, refer to Liang (2016) and Liang and Anderson (2007). In Xu and Liang (2017), there is a brief comparison to the traditional energetics in the Reynolds framework.

A.1 *Multiscale window transform*

As is well known, multiscale energetics formulated with time mean (resp. zonal mean) do not have information in time (resp. longitude). These formalisms, or Reynolds decomposition-based formalisms as called, cannot be used to study the energy burst processes which are generally localized in space and time. During past decades, a common practice is to use filtering to replace the time averaging in these formalisms. For example, application of a low-pass filter to a velocity field *u(t)* yields a slowly varying $\overline{u}(t)$, and a high-pass filter to it gives a fast varying eddy part $u'(t)$: $u(t) = \overline{u}(t) + u'(t)$. Now time dependence is retained in both fields, and hence seemingly the local information is retained. Entailing is, however, a very basic physical question: What are the mean energy and eddy energy with this decomposition? When $\overline{u}$ is time invariant, this is a Reynolds decomposition, we know the eddy energy is $\overline{[u'(t)]^2}$; now if $\overline{u}$ is time varying, what is the eddy energy then? During the past 2-3 decades, a common practice in the literature is simply to take it as $[u'(t)]^2$. That corresponds to, in the Reynolds decomposition case, a relieving of the time mean in the eddy energy $\overline{[u'(t)]^2}$.

This is, unfortunately, conceptually incorrect. To illustrate, consider a very simple example which has a Fourier expansion

$$u(t) = \overline{u}(t) + u'(t) = [a_0 \cos\omega_0 t] + [a_1 \cos\omega_1 t],\ \omega_1 > \omega_0,$$

with subscripts 0, 1 representing the slow and fast processes, respectively. Now what are the energies for these processes? In this simple case we know they should be, respectively, a_0^2 and a_1^2. That is to say, multiscale energy is a concept in phase space; here they are functions of the Fourier coefficients (a_0, a_1). By the common practice with

filters as shown above, however, the energies would be simply taken as

$$[\bar{u}(t)]^2 = [a_0 \cos\omega_0 t]^2 \text{ and } [u'(t)]^2 = [a_1 \cos\omega_1 t]^2$$

which are functions of the reconstructions or filtered parts in physical space!

So the common practice during the past decades is conceptually incorrect. Multiscale energy is a concept in phase space; it is related to its physical space counterpart through the famous Parseval equality. Mathematically it is the square of the norm of a field variable, or, alternatively, the Fourier transform of an autocorrelation function (e.g., Batchelor, 1953). In the above example, when $\omega_0 = 0$, it is easy to prove that ${a_1}^2 = \overline{[u'(t)]^2}$, just as that with the Reynolds decomposition. From this example *one also sees that the time mean in the classical Reynolds formalism is essential; it cannot be removed to pretend to gain the time variability*. In fact, it is by no means a trivial task to have the local energy of a time-dependent filtered field faithfully represented; it is a rather profound problem. This even has not been possible until filter banks and wavelets are connected (Strang and Nguyen, 1996), and has just been systematically addressed by Liang and Anderson (2007) in the development of multiscale window transform (MWT).

MWT is a tool that helps decompose a function space into a direct sum of orthogonal subspaces, each with an exclusive range of scales (represented by wavelet scale levels), while having the local information retained. Such a subspace is termed a *scale window*, or simply a window. MWT can be viewed as a generalization of the classical Reynolds decomposition; originally it is developed for representing the energies (and any quadratic quantities) on the resulting scale windows, in order to make multiscale

energetics analysis possible. Liang and Anderson (2007) find that, for some specially constructed orthogonal[1] filters, there exists a transfer-reconstruction pair, namely, MWT and its counterpart multiscale window reconstruction (MWR). In some sense MWR functions just like a filter in the traditional sense. What makes it different is that, for each MWR, there exists an MWT which gives coefficients that can be used to represent the energy of the filtered series. In this way multiscale energetics analysis is made possible.

In MWT, a scale window is demarcated by two scale levels, or window bounds. For a time series with a duration τ, a scale level j corresponds to a period $2^{-j}\tau$. In the M-window case, the windows are bounded above by $M+1$ scale levels: $j_0, j_1, \ldots, j_M$. Alternatively, $2^{-j_0}\tau, 2^{-j_1}\tau, \ldots, 2^{-j_M}\tau$ are the time scale bounds. For convenience, we will denote them by $\varpi = 0, 1, ..., M$ respectively.

Now suppose $\{\varphi_n^j(t)\}_n$ is an orthonormal translational invariant scaling sequence (built from cubic splines; see Liang and Anderson (2007), and Figure 1 in Liang (2016)), with j some wavelet scale level and n the time step. Let $T(t)$ be some square integrable function defined on [0,1] (if not, the domain can always be rescaled to [0,1]). It has been shown (Liang and Anderson 2007) that all such functions can be practically represented using $\{\varphi_n^j(t)\}_n$ as a basis. In doing this, there is a scaling transform

$$\hat{T}_n^j = \int_0^1 T(t)\varphi_n^j(t)dt$$

[1] Note here *orthogonality* is crucial; otherwise Parseval's relation does not hold and hence energy cannot even be defined.

for any scale level j (corresponding to frequency 2^j). Given window bounds j_0, j_1 for a two–window decomposition, T then can be reconstructed on the windows formed above:

$$T^{\sim 0}(t) = \sum_{n=0}^{2^{j_0}-1} \hat{T}_n^{j_0} \varphi_n^{j_0}(t),$$

$$T^{\sim 1}(t) = \sum_{n=0}^{2^{j_1}-1} \hat{T}_n^{j_1} \varphi_n^{j_1}(t) - T^{\sim 0}(t),$$

with the notations ~0, ~1 signifying the corresponding scale windows. With these reconstructions (multiscale window reconstruction, or MWR for short), the MWT of T is defined as

$$\hat{T}_n^{\sim \varpi} = \int_0^1 T^{\sim \varpi}(t) \varphi_n^{j_1}(t) dt,$$

for windows $\varpi = 0,1$ and $n = 0,1,\cdots,N$, and $N = 2^{j_1} - 1$. In terms of $\hat{T}^{\sim \varpi}$ the above reconstructions on the two windows can be written in a unified way:

$$T^{\sim \varpi}(t) = \sum_{n=0}^{2^{j_1}-1} \hat{T}_n^{\sim \varpi} \varphi_n^{j_1}(t).$$

These two equations make a transform-reconstruction pair for the MWT. Note that the $T^{\sim \varpi}(t)$ are just like the low/high-pass filtered quantities which are defined in physical space, while the transform coefficients $\hat{T}_n^{\sim \varpi}$ (just like Fourier coefficients) can be used to represent multiscale energy---it has been rigorously proved that the energy on scale ϖ is precisely equal to the square of the MWT coefficients (up to some constant multiplier). Note it is by no means as trivial as $[T^{\sim \varpi}(t)]^2$, which has been frequently seen in the literature.

A.2 Multiscale energetics and local Lorenz cycle

Following Liang (2016), consider the primitive equations in an isobaric coordinate frame:

$$\frac{\partial \mathbf{v}_h}{\partial t} + \mathbf{v}_h \cdot \nabla_h \mathbf{v}_h + \omega \frac{\partial \mathbf{v}_h}{\partial p} + f\mathbf{k} \times \mathbf{v}_h = -\nabla_h \Phi + \mathbf{F} \tag{A1}$$

$$\frac{\partial \Phi}{\partial p} = -\alpha \tag{A2}$$

$$\nabla_h . \mathbf{v}_h + \frac{\partial \omega}{\partial p} = 0 \tag{A3}$$

$$\frac{\partial T}{\partial t} + \mathbf{v}_h \cdot \nabla_h \mathrm{T} + \omega \frac{\partial T}{\partial p} + \omega \bar{\alpha} \frac{L - L_d}{g} + \omega \alpha \frac{L - L_d}{g} = \frac{\dot{q}_{net}}{c_p} \tag{A4}$$

$$p\alpha = RT \tag{A5}$$

where L is the lapse rate and L_d the lapse rate for dry air, the subscript h stands for horizontal direction and the overbar for mean over time and over the isobaric plane. The other notations are conventional. Note here Φ (geopotential) and α (specific volume) are anomalies; their time averages have been pre-subtracted.

With MWT, the available potential energy (APE) and kinetic energy (KE) densities (for convenience, we will simply refer to them as APE and KE, unless confusion may arise) on window ϖ at location n can be defined, following Lorenz (1955), as

$$A^{\varpi} = \frac{1}{2} c \left(\hat{T}^{\sim \varpi}\right)^2, \tag{A6}$$

$$K^{\varpi} = \frac{1}{2} \hat{\boldsymbol{v}}_{\mathrm{h}}^{\sim \varpi} \cdot \hat{\boldsymbol{v}}_{\mathrm{h}}^{\sim \varpi}. \tag{A7}$$

Note here the subscript n has been suppressed for clarity; same below. From Eqs. (A1)-(A5) the evolutionary equations for K^{ϖ} and A^{ϖ} for windows ϖ (=0, 1, …) can be obtained; they are Eqs. (1) and (2), which we rewrite as follows:

$$\frac{\partial K^{\varpi}}{\partial t} + \nabla \cdot \mathbf{Q}_K^{\varpi} = \Gamma_K^{\varpi} - \nabla \cdot \mathbf{Q}_P^{\varpi} + b^{\varpi} + \mathrm{F}_K^{\varpi} \tag{A8}$$

$$\frac{\partial A^{\varpi}}{\partial t} + \nabla \cdot \mathbf{Q}_A^{\varpi} = \Gamma_A^{\varpi} - b^{\varpi} + S_A^{\varpi} + F_A^{\varpi} \quad \text{(A9)}$$

The physical explanations and mathematical expressions for these terms are listed in Table A1.

Table A1. The energetic terms in Equations (A8)-(A9). The colon operator (:) in Γ_K^{ϖ} and Γ_A^{ϖ} is defined such that, for two dyadic products **AB** and **CD**, $(\mathbf{AB}):(\mathbf{CD}) = (\mathbf{A}\cdot\mathbf{C})(\mathbf{B}\cdot\mathbf{D})$. If total energetics (in W) are to be computed, the resulting integrals with respect to (*x, y, p*) should be divided by *g*. Besides, all terms are to be multiplied by 2^{j_1}, which is omitted for notational simplicity.

Symbol	Mathematical expression	Physical interpretation
K^{ϖ}	$\frac{1}{2}\hat{\mathbf{v}}_h^{\sim\varpi}\cdot\hat{\mathbf{v}}_h^{\sim\varpi}$	KE on scale window ϖ
$\boldsymbol{Q}_K^{\varpi}$	$\frac{1}{2}\widehat{(\mathbf{v}\mathbf{v}_h)}^{\sim\varpi}\cdot\hat{\mathbf{v}}_h^{\sim\varpi}$	Flux of KE on window ϖ
Γ_K^{ϖ}	$\frac{1}{2}[\widehat{(\mathbf{v}\mathbf{v}_h)}^{\sim\varpi}:\nabla\hat{\mathbf{v}}_h^{\sim\varpi} - \nabla\cdot\widehat{(\mathbf{v}\mathbf{v}_h)}^{\sim\varpi}\cdot\hat{\mathbf{v}}_h^{\sim\varpi}]$	Canonical transfer of KE to window ϖ
$\boldsymbol{Q}_P^{\varpi}$	$\hat{\mathbf{v}}^{\sim\varpi}\hat{\Phi}^{\sim\varpi}$	Geopotential flux
b^{ϖ}	$-\hat{\omega}^{\sim\varpi}\hat{\alpha}^{\sim\varpi}$	Buoyancy conversion
A^{ϖ}	$\frac{1}{2}c(\hat{\mathrm{T}}^{\sim\varpi})^2, c = \frac{g}{\overline{T}(g/C_p - L)}$	APE on scale window ϖ
$\boldsymbol{Q}_A^{\varpi}$	$\frac{1}{2}c\hat{\mathrm{T}}^{\sim\varpi}\widehat{(\mathbf{v}\mathrm{T})}^{\sim\varpi}$	Flux of APE on window ϖ
Γ_A^{ϖ}	$\frac{c}{2}[\widehat{(\mathbf{v}\mathrm{T})}^{\sim\varpi}\cdot\nabla\hat{\mathrm{T}}^{\sim\varpi} - \hat{\mathrm{T}}^{\sim\varpi}\nabla\cdot\widehat{(\mathbf{v}\mathrm{T})}^{\sim\varpi}]$	Canonical transfer of APE to window ϖ
S_A^{ϖ}	$\frac{1}{2}\hat{\mathrm{T}}^{\sim\varpi}\widehat{(\omega\mathrm{T})}^{\sim\varpi}\frac{\partial c}{\partial p} + \frac{1}{\overline{T}}\widehat{\omega\alpha}^{\sim\varpi}$	Apparent source/sink (usually negligible)

Among those terms in Table A1 are $\Gamma_{\mathrm{A}}^{\varpi}$ and $\Gamma_{\mathrm{K}}^{\varpi}$, which represent the transfers of APE and KE between the scale windows and hence make the processes that we are most interested in for this study. For a scalar field T (may be any scalar field or component of vector field; not necessarily temperature) in a flow $\boldsymbol{v}$, the energy transfer from other scale windows to window ϖ is (see Liang (2016) for a rigorous proof)

$$\Gamma_n^{\varpi} = -E_n^{\varpi}\nabla\cdot\boldsymbol{v}_{\mathrm{T}}^{\varpi} = \frac{1}{2}\left[\widehat{(\boldsymbol{v}T)}_n^{\sim\varpi}\cdot\nabla\hat{T}_n^{\sim\varpi} - \hat{T}_n^{\sim\varpi}\nabla\cdot\widehat{(\boldsymbol{v}T)}_n^{\sim\varpi}\right], \tag{A10}$$

where $E^{\varpi} = \frac{1}{2}(\hat{T}^{\sim\varpi})^2$ is the energy of window ϖ.[1] The other symbol

$$\boldsymbol{v}_{\mathrm{T}}^{\varpi} = \frac{\widehat{(T\boldsymbol{v})}_n^{\sim\varpi}}{\hat{T}_n^{\sim\varpi}} \tag{A11}$$

is referred to as the *T-coupled velocity*, which can be understood as the weighted average of $\boldsymbol{v}$ in the phase space of MWT. With this, the transfer of APE and KE can be easily obtained. For example,

$$\Gamma_{\mathrm{K}}^{\varpi} = -\frac{1}{2}\left[(\hat{u}^{\sim\varpi})^2\nabla\cdot\boldsymbol{v}_{\mathrm{u}}^{\varpi} + (\hat{v}^{\sim\varpi})^2\nabla\cdot\boldsymbol{v}_{\mathrm{v}}^{\varpi}\right] \tag{A12}$$

which can be proved to be that in Table A1.

The so-obtained transfer possesses a very interesting property, namely

$$\sum_{\varpi}\sum_{n}\Gamma_n^{\varpi} = 0, \tag{A13}$$

as first proposed in Liang and Robinson (2005) and later proved in Liang (2016). Physically, this implies that the transfer is a mere redistribution of energy among the scale windows, without generating or destroying energy as a whole. This property,

[1] When needed, a constant should be multiplied on both sides. For example, if T is temperature, then E^{ϖ} and Γ^{ϖ} should be both multiplied by c to make APE and APE transfer.

though simple to state, does not hold in previous time decomposition-based or Lorenz-type energetics formalisms (refer to Liang and Robinson (2007) for a clear comparison to the classical formalism). To distinguish it from those that may have been encountered in the literature, it is termed *canonical transfer*.

As shown in Liang (2016), a canonical transfer has a *Lie bracket form*; it satisfies the *Jacobian identity*, reminiscent of the *Poisson bracket in Hamiltonian mechanics*. It also satisfies a "*detailed balance relation*", which usually results from the Saltzman-type or space decomposition-based energetics formalisms (Liang and Robinson 2005).

So, for an ideal fluid, the energetic processes represented in (A8)-(A9) are all conservative. In other words, a local Lorenz cycle in the absence of dissipation and diffusion is composed of the following three types of processes:

- transports: redistributing energy in space (vanishing if integrated over a closed domain),
- canonical transfers: redistributing energy among scale windows (vanishing if summarized over scale windows and locations),
- buoyancy conversion: redistributing energy between APE and KE.

Figure A1 schematizes these processes for a two-window decomposition. Note here the arrows connecting $K^0(A^0)$ and $K^1(A^1)$ are the quantities that are difficult to diagnose with the traditional methods.

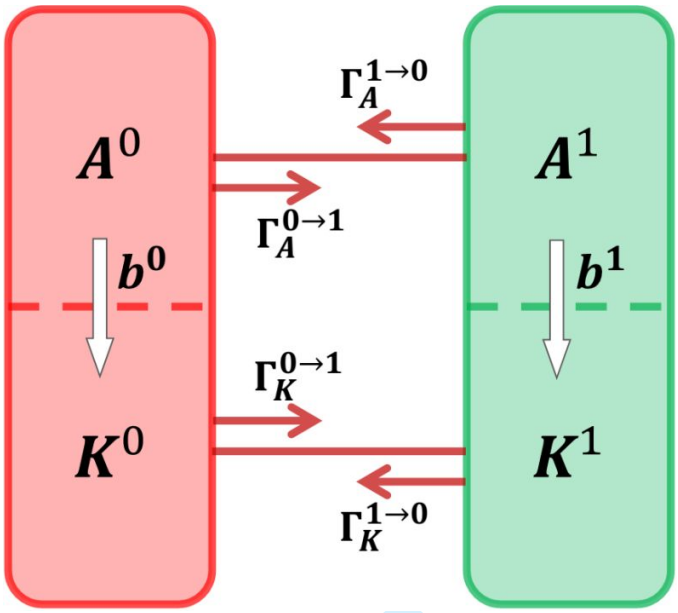

Figure A1. The local Lorenz cycle for a two-window decomposition (the scale windows are denoted in the superscripts as 0 and 1, respectively). For clarity, transports and dissipative/diffusive processes are not shown.

Note a canonical transfer may involve contributions from essentially all scale windows; it is necessary to differentiate them. Consider for an example window $\varpi = 1$. The energy transferred to the window can be from window 0 and itself $\varpi = 1$. Since all canonical transfers are linear combinations of terms in a triple product form:

$$\Gamma_{\mathrm{n}}^{1} = \hat{\mathcal{R}}_n^{\sim 1}(\widehat{pq})_n^{\sim 1}$$

it suffices to consider Γ_{n}^{1}. From Liang (2016), it is

$$\Gamma_{\mathrm{n}}^{1} = \hat{\mathcal{R}}_n^{\sim 1}\left[(\widehat{p^{\sim 0}q^{\sim 0}})_n^{\sim 1} + (\widehat{p^{\sim 0}q^{\sim 1}})_n^{\sim 1} + (\widehat{p^{\sim 1}q^{\sim 0}})_n^{\sim 1}\right] + \hat{\mathcal{R}}_n^{\sim 1}(\widehat{p^{\sim 1}q^{\sim 1}})_n^{\sim 1}$$

where the first part on the right hand side is the canonical energy transfer from window 0 to window 1; write it as $\Gamma^{0\to1}$. The second part, denoted by $\Gamma^{1\to1}$, is the canonical energy transfer to itself, which is usually very small. $\Gamma^{0\to1}$ is of particular importance in that it

is usually related to the instability in geophysical fluid dynamics; in particular, $\Gamma_A^{0\to1}$ and $\Gamma_K^{0\to1}$ are usually related to baroclinic instability and barotropic instability of the mean flow. For this reason, in the text sometimes $\Gamma_A^{0\to1}$ and $\Gamma_K^{0\to1}$ have been referred to as baroclinic canonical transfer and barotropic canonical transfer, respectively.

Acknowledgements

The suggestions of two anonymous reviewers are sincerely appreciated. This study was partially supported by the Jiangsu Provincial Government through the 2015 Jiangsu Program for Innovation Research and Entrepreneurship Groups and the Jiangsu Chair Professorship to XSL, the National Natural Science Foundation of China under Grants No. 41276032 and 41705024, and the National Program on Global Change and Air-Sea Interaction [GASI-IPOVAI-06].

References

Anderson, D., Hodges, K.I., Hoskins, B.J., 2003. Sensitivity of Feature-Based Analysis Methods of Storm Tracks to the Form of Background Field Removal. Mon. Weather Rev. 131, 565–573. https://doi.org/10.1175/1520-0493(2003)131<0565:SOFBAM>2.0.CO;2

Andrews, D.G., McIntyre, M.E., 1978. Generalized Eliassen-Palm and Charney-Drazin Theorems for Waves on Axismmetric Mean Flows in Compressible Atmospheres. J. Atmospheric Sci. 35, 175–185. https://doi.org/10.1175/1520-0469(1978)035<0175:GEPACD>2.0.CO;2

Barnes, E.A., Hartmann, D.L., 2011. Rossby Wave Scales, Propagation, and the Variability of Eddy-Driven Jets. J. Atmospheric Sci. 68, 2893–2908. https://doi.org/10.1175/JAS-D-11-039.1

Barnes, J.R., Young, R.E., 1992. Nonlinear Baroclinic Instability on the Sphere: Multiple Life Cycles with Surface Drag and Thermal Damping. J. Atmospheric Sci. 49,

861–878. https://doi.org/10.1175/1520-0469(1992)049<0861:NBIOTS>2.0.CO;2

Bengtsson, L., Hodges, K.I., Esch, M., Keenlyside, N., Kornblueh, L., Luo, J.-J., Yamagata, T., 2007. How may tropical cyclones change in a warmer climate? Tellus A 59, 539–561. https://doi.org/10.1111/j.1600-0870.2007.00251.x

Bengtsson, L., Hodges, K.I., Keenlyside, N., 2009. Will Extratropical Storms Intensify in a Warmer Climate? J. Clim. 22, 2276–2301. https://doi.org/10.1175/2008JCLI2678.1

Blackmon, M.L., 1976. A Climatological Spectral Study of the 500 mb Geopotential Height of the Northern Hemisphere. J. Atmospheric Sci. 33, 1607–1623. https://doi.org/10.1175/1520-0469(1976)033<1607:ACSSOT>2.0.CO;2

Blackmon, M.L., Lee, Y.-H., Wallace, J.M., 1984. Horizontal Structure of 500 mb Height Fluctuations with Long, Intermediate and Short Time Scales. J. Atmospheric Sci. 41, 961–980. https://doi.org/10.1175/1520-0469(1984)041<0961:HSOMHF>2.0.CO;2

Blackmon, M.L., Wallace, J.M., Lau, N.-C., Mullen, S.L., 1977. An Observational Study of the Northern Hemisphere Wintertime Circulation. J. Atmospheric Sci. 34, 1040–1053. https://doi.org/10.1175/1520-0469(1977)034<1040:AOSOTN>2.0.CO;2

Cai, M., M. Mak, 1990. On the Basic Dynamics of Regional Cyclogenesis. J. Atmospheric Sci., 47, 1417–1442, doi:10.1175/1520-0469(1990)047<1417:OTBDOR>2.0.CO;2.

Catto, J.L., Shaffrey, L.C., Hodges, K.I., 2010. Can Climate Models Capture the Structure of Extratropical Cyclones? J. Clim. 23, 1621–1635. https://doi.org/10.1175/2009JCLI3318.1

Chang, E.K.M., 2001a. GCM and Observational Diagnoses of the Seasonal and Interannual Variations of the Pacific Storm Track during the Cool Season. J. Atmospheric Sci. 58, 1784–1800. https://doi.org/10.1175/1520-0469(2001)058<1784:GAODOT>2.0.CO;2

Chang, E. K. M., 2001b. The Structure of Baroclinic Wave Packets. J. Atmospheric Sci., 58, 1694–1713, doi:10.1175/1520-0469(2001)058<1694:TSOBWP>2.0.CO;2.

Chang, E.K.M., 1993. Downstream Development of Baroclinic Waves As Inferred from Regression Analysis. J. Atmospheric Sci. 50, 2038–2053. https://doi.org/10.1175/1520-0469(1993)050<2038:DDOBWA>2.0.CO;2

Chang, E.K.M., Lee, S., Swanson, K.L., 2002. Storm Track Dynamics. J. Clim. 15, 2163–2183. https://doi.org/10.1175/1520-0442(2002)015<02163:STD>2.0.CO;2

Chang, E.K.M., Orlanski, I., 1993. On the Dynamics of a Storm Track. J. Atmospheric Sci. 50, 999–1015. https://doi.org/10.1175/1520-0469(1993)050<0999:OTDOAS>2.0.CO;2

Charney, J.G., Drazin, P.G., 1961. Propagation of planetary-scale disturbances from the lower into the upper atmosphere. J. Geophys. Res. 66, 83–109. https://doi.org/10.1029/JZ066i001p00083

Chen, G., Plumb, R.A., 2009. Quantifying the Eddy Feedback and the Persistence of the Zonal Index in an Idealized Atmospheric Model. J. Atmospheric Sci. 66, 3707–3720. https://doi.org/10.1175/2009JAS3165.1

Dacre, H.F., Hawcroft, M.K., Stringer, M.A., Hodges, K.I., 2012. An Extratropical Cyclone Atlas: A Tool for Illustrating Cyclone Structure and Evolution Characteristics. Bull. Am. Meteorol. Soc. 93, 1497–1502. https://doi.org/10.1175/BAMS-D-11-00164.1

Deng, Y., Mak, M., 2006. Nature of the Differences in the Intraseasonal Variability of the Pacific and Atlantic Storm Tracks: A Diagnostic Study. J. Atmospheric Sci. 63, 2602–2615. https://doi.org/10.1175/JAS3749.1

Dickinson, R.E., 1969. Theory of Planetary Wave-Zonal Flow Interaction. J. Atmospheric Sci. 26, 73–81. https://doi.org/10.1175/1520-0469(1969)026<0073:TOPWZF>2.0.CO;2

Edmon, H.J., Hoskins, B.J., McIntyre, M.E., 1980. Eliassen-Palm Cross Sections for the Troposphere. J. Atmospheric Sci. 37, 2600–2616. https://doi.org/10.1175/1520-0469(1980)037<2600:EPCSFT>2.0.CO;2

Eliassen, A., Palm, E., 1961. On the transfer of energy in stationary mountain waves. Geofys Publ 22, 1–23.

Farrell, B., 1984. Modal and Non-Modal Baroclinic Waves. J. Atmospheric Sci., 41, 668–673, doi:10.1175/1520-0469(1984)041<0668:MANMBW>2.0.CO;2.

——, 1985. Transient Growth of Damped Baroclinic Waves. J. Atmospheric Sci., 42, 2718–2727, doi:10.1175/1520-0469(1985)042<2718:TGODBW>2.0.CO;2.

——, 1989. Optimal Excitation of Baroclinic Waves. J. Atmospheric Sci., 46, 1193–1206, doi:10.1175/1520-0469(1989)046<1193:OEOBW>2.0.CO;2.

Field, P.R., Wood, R., 2007. Precipitation and Cloud Structure in Midlatitude Cyclones. J. Clim. 20, 233–254. https://doi.org/10.1175/JCLI3998.1

Franzke, C., Woollings, T., Martius, O., 2011. Persistent Circulation Regimes and Preferred Regime Transitions in the North Atlantic. J. Atmospheric Sci. 68, 2809–2825. https://doi.org/10.1175/JAS-D-11-046.1

Gerber, E.P., Vallis, G.K., 2007. Eddy–Zonal Flow Interactions and the Persistence of the Zonal Index. J. Atmospheric Sci. 64, 3296–3311. https://doi.org/10.1175/JAS4006.1

Green, J.S.A., 1960. A problem in baroclinic stability. Q. J. R. Meteorol. Soc. 86, 237–251. https://doi.org/10.1002/qj.49708636813

Harnik, N., Chang, E.K.M., 2004. The Effects of Variations in Jet Width on the Growth of Baroclinic Waves: Implications for Midwinter Pacific Storm Track Variability. J. Atmospheric Sci. 61, 23–40. https://doi.org/10.1175/1520-0469(2004)061<0023:TEOVIJ>2.0.CO;2

Hartmann, D.L., 1974. Time Spectral Analysis of Mid-Latitude Disturbances. Mon. Weather Rev. 102, 348–362. https://doi.org/10.1175/1520-0493(1974)102<0348:TSAOML>2.0.CO;2

Hodges, K.I., 1995. Feature Tracking on the Unit Sphere. Mon. Weather Rev. 123, 3458–3465. https://doi.org/10.1175/1520-0493(1995)123<3458:FTOTUS>2.0.CO;2

Hoskins, B.J., McIntyre, M.E., Robertson, A.W., 1985. On the use and significance of isentropic potential vorticity maps. Q. J. R. Meteorol. Soc. 111, 877–946. https://doi.org/10.1002/qj.49711147002

Hoskins, B.J., Valdes, P.J., 1990. On the Existence of Storm-Tracks. J. Atmospheric Sci. 47, 1854–1864. https://doi.org/10.1175/1520-0469(1990)047<1854:OTEOST>2.0.CO;2

James, I. N., 1987. Suppression of Baroclinic Instability in Horizontally Sheared Flows. J. Atmospheric Sci., 44, 3710–3720, doi:10.1175/1520-0469(1987)044<3710:SOBIIH>2.0.CO;2.

Kidston, J., Frierson, D.M.W., Renwick, J.A., Vallis, G.K., 2010. Observations, Simulations, and Dynamics of Jet Stream Variability and Annular Modes. J. Clim. 23, 6186–6199. https://doi.org/10.1175/2010JCLI3235.1

Kidston, J., Vallis, G.K., 2012. The Relationship between the Speed and the Latitude of an Eddy-Driven Jet in a Stirred Barotropic Model. J. Atmospheric Sci. 69, 3251–3263. https://doi.org/10.1175/JAS-D-11-0300.1

Lau, N.-C., 1979. The Structure and Energetics of Transient Disturbances in the Northern Hemisphere Wintertime Circulation. J. Atmospheric Sci. 36, 982–995. https://doi.org/10.1175/1520-0469(1979)036<0982:TSAEOT>2.0.CO;2

Lee, S., Kim, H., 2003. The Dynamical Relationship between Subtropical and Eddy-Driven Jets. J. Atmospheric Sci. 60, 1490–1503. https://doi.org/10.1175/1520-0469(2003)060<1490:TDRBSA>2.0.CO;2

Li, C., Wettstein, J.J., 2011. Thermally Driven and Eddy-Driven Jet Variability in Reanalysis. J. Clim. 25, 1587–1596. https://doi.org/10.1175/JCLI-D-11-00145.1

Liang, X.S., 2016. Canonical Transfer and Multiscale Energetics for Primitive and Quasigeostrophic Atmospheres. J. Atmospheric Sci. 73, 4439–4468. https://doi.org/10.1175/JAS-D-16-0131.1

Liang, X.S., Anderson, D.G.M., 2007. Multiscale Window Transform. Multiscale Model. Simul. 6, 437–467. https://doi.org/10.1137/06066895X

Liang, X.S., Robinson, A.R., 2007. Localized multi-scale energy and vorticity analysis. Dyn. Atmospheres Oceans 44, 51–76. https://doi.org/10.1016/j.dynatmoce.2007.04.001

Liang, X.S., Robinson, A.R., 2005. Localized multiscale energy and vorticity analysis. Dyn. Atmospheres Oceans 38, 195–230. https://doi.org/10.1016/j.dynatmoce.2004.12.004

Lim, G.H., Wallace, J.M., 1991. Structure and Evolution of Baroclinic Waves as Inferred from Regression Analysis. J. Atmospheric Sci. 48, 1718–1732. https://doi.org/10.1175/1520-0469(1991)048<1718:SAEOBW>2.0.CO;2

Lindzen, R.S., Farrell, B., 1980. A Simple Approximate Result for the Maximum Growth Rate of Baroclinic Instabilities. J. Atmospheric Sci. 37, 1648–1654.

https://doi.org/10.1175/1520-0469(1980)037<1648:ASARFT>2.0.CO;2
Lindzen, R.S., Holton, J.R., 1968. A Theory of the Quasi-Biennial Oscillation. J. Atmospheric Sci. 25, 1095–1107. https://doi.org/10.1175/1520-0469(1968)025<1095:ATOTQB>2.0.CO;2
Lorenz, D.J., 2014. Understanding Midlatitude Jet Variability and Change Using Rossby Wave Chromatography: Wave–Mean Flow Interaction. J. Atmospheric Sci. 71, 3684–3705. https://doi.org/10.1175/JAS-D-13-0201.1
Lorenz, D.J., Hartmann, D.L., 2001. Eddy–Zonal Flow Feedback in the Southern Hemisphere. J. Atmospheric Sci. 58, 3312–3327. https://doi.org/10.1175/1520-0469(2001)058<3312:EZFFIT>2.0.CO;2
Lorenz, E.N., 1955. Available Potential Energy and the Maintenance of the General Circulation. Tellus 7, 157–167. https://doi.org/10.1111/j.2153-3490.1955.tb01148.x
Ma, J., X.S. Liang, 2017. Multiscale dynamical processes underlying the wintertime Atlantic blockings. J. Atmos. Sci., 74, 3815-3831.
Mak, M., M. Cai, 1989. Local Barotropic Instability. J. Atmospheric Sci., 46, 3289–3311, doi:10.1175/1520-0469(1989)046<3289:LBI>2.0.CO;2.
Nakamura, H., 1992. Midwinter Suppression of Baroclinic Wave Activity in the Pacific. J. Atmospheric Sci. 49, 1629–1642. https://doi.org/10.1175/1520-0469(1992)049<1629:MSOBWA>2.0.CO;2
Novak, L., Ambaum, M.H.P., Tailleux, R., 2015. The Life Cycle of the North Atlantic Storm Track. J. Atmospheric Sci. 72, 821–833. https://doi.org/10.1175/JAS-D-14-0082.1
Orlanski, I., Chang, E.K.M., 1993. Ageostrophic Geopotential Fluxes in Downstream and Upstream Development of Baroclinic Waves. J. Atmospheric Sci. 50, 212–225. https://doi.org/10.1175/1520-0469(1993)050<0212:AGFIDA>2.0.CO;2
Orlanski, I., Katzfey, J., 1991. The Life Cycle of a Cyclone Wave in the Southern Hemisphere. Part I: Eddy Energy Budget. J. Atmospheric Sci. 48, 1972–1998. https://doi.org/10.1175/1520-0469(1991)048<1972:TLCOAC>2.0.CO;2
Papritz, L., S. Schemm, 2013. Development of an idealised downstream cyclone: Eulerian and Lagrangian perspective on the kinetic energy. Tellus Dyn. Meteorol. Oceanogr., 65, 19539, doi:10.3402/tellusa.v65i0.19539.
Penny, S.M., Battisti, D.S., Roe, G.H., 2013. Examining Mechanisms of Variability within the Pacific Storm Track: Upstream Seeding and Jet-Core Strength. J. Clim. 26, 5242–5259. https://doi.org/10.1175/JCLI-D-12-00017.1
Pierrehumbert, R.T., Swanson, K.L., 1995. Baroclinic Instability. Annu. Rev. Fluid Mech. 27, 419–467. https://doi.org/10.1146/annurev.fl.27.010195.002223
Plumb, R. A., 1983. A New Look at the Energy Cycle. J. Atmospheric Sci., 40, 1669–1688, doi:10.1175/1520-0469(1983)040<1669:ANLATE>2.0.CO;2.
Plumb, R.A., 1985. An Alternative Form of Andrews' Conservation Law for Quasi-geostrophic Waves on a Steady, Nonuniform Flow. J. Atmospheric Sci. 42,

298–300. https://doi.org/10.1175/1520-0469(1985)042<0298:AAFOAC>2.0.CO;2

Rivière, G., B. L. Hua, P. Klein, 2003. Perturbation growth in terms of barotropic alignment properties. Q. J. R. Meteorol. Soc., 129, 2613–2635, doi:10.1256/qj.02.106.

——, ——, and ——, 2004: Perturbation growth in terms of baroclinic alignment properties. Q. J. R. Meteorol. Soc., 130, 1655–1673, doi:10.1256/qj.02.223.

Rivière, G., P. Arbogast, A. Joly, 2015. Eddy kinetic energy redistribution within idealized extratropical cyclones using a two-layer quasi-geostrophic model: Eddy kinetic energy redistribution within idealized extratropical cyclones using a two-layer quasi-geostrophic model. Q. J. R. Meteorol. Soc., 141, 207–223, doi:10.1002/qj.2350.

Robinson, W.A., 2000. A Baroclinic Mechanism for the Eddy Feedback on the Zonal Index. J. Atmospheric Sci. 57, 415–422. https://doi.org/10.1175/1520-0469(2000)057<0415:ABMFTE>2.0.CO;2

Simmons, A.J., Hoskins, B.J., 1980. Barotropic Influences on the Growth and Decay of Nonlinear Baroclinic Waves. J. Atmospheric Sci. 37, 1679–1684. https://doi.org/10.1175/1520-0469(1980)037<1679:BIOTGA>2.0.CO;2

Simmons, A.J., Hoskins, B.J., 1978. The Life Cycles of Some Nonlinear Baroclinic Waves. J. Atmospheric Sci. 35, 414–432. https://doi.org/10.1175/1520-0469(1978)035<0414:TLCOSN>2.0.CO;2

Sinclair, M.R., Revell, M.J., 2000. Classification and Composite Diagnosis of Extratropical Cyclogenesis Events in the Southwest Pacific. Mon. Weather Rev. 128, 1089–1105. https://doi.org/10.1175/1520-0493(2000)128<1089:CACDOE>2.0.CO;2

Uppala, S.M., KÅllberg, P.W., Simmons, A.J., Andrae, U., Bechtold, V.D.C., Fiorino, M., Gibson, J.K., Haseler, J., Hernandez, A., Kelly, G.A., Li, X., Onogi, K., Saarinen, S., Sokka, N., Allan, R.P., Andersson, E., Arpe, K., Balmaseda, M.A., Beljaars, A.C.M., Berg, L.V.D., Bidlot, J., Bormann, N., Caires, S., Chevallier, F., Dethof, A., Dragosavac, M., Fisher, M., Fuentes, M., Hagemann, S., Hólm, E., Hoskins, B.J., Isaksen, L., Janssen, P. a. E.M., Jenne, R., Mcnally, A.P., Mahfouf, J.-F., Morcrette, J.-J., Rayner, N.A., Saunders, R.W., Simon, P., Sterl, A., Trenberth, K.E., Untch, A., Vasiljevic, D., Viterbo, P., Woollen, J., 2005. The ERA-40 re-analysis. Q. J. R. Meteorol. Soc. 131, 2961–3012. https://doi.org/10.1256/qj.04.176

Vallis, G.K., Gerber, E.P., 2008. Local and hemispheric dynamics of the North Atlantic Oscillation, annular patterns and the zonal index. Dyn. Atmospheres Oceans, Current Contributions to Understanding the General Circulation of the Atmosphere Part 2 44, 184–212. https://doi.org/10.1016/j.dynatmoce.2007.04.003

Woollings, T., Hannachi, A., Hoskins, B., 2010. Variability of the North Atlantic eddy-driven jet stream. Q. J. R. Meteorol. Soc. 136, 856–868.

https://doi.org/10.1002/qj.625

Xu, F., Liang, X.S., 2017. On the generation and maintenance of the 2012/13 sudden stratospheric warming. J. Atmos. Sci., 74, 3209-3228.

Zhang, Y., Yang, X.-Q., Nie, Y., Chen, G., 2012. Annular Mode–Like Variation in a Multilayer Quasigeostrophic Model. J. Atmospheric Sci. 69, 2940–2958. https://doi.org/10.1175/JAS-D-11-0214.1

Zhao, Y.-B., Liang X.S., 2018. On the inverse relationship between the boreal wintertime Pacific jet strength and storm-track intensity. J. Climate, https://doi.org/10.1175/JCLI-D-18-0043.1, in press.